Toward the feldspar alternative for cosmogenic [10]Be applications

Swann Zerathe [a, d, *], Pierre-Henri Blard [b], Régis Braucher [c], Didier Bourlès [c], Laurence Audin [a], Julien Carcaillet [a], Fabrizio Delgado [d], Carlos Benavente [d], ASTER Team[1]

[a] Univ. Grenoble Alpes, Univ. Savoie Mont Blanc, CNRS, IRD, IFSTTAR, ISTerre, 38000 Grenoble, France
[b] CRPG, UMR7358, CNRS, Université de Lorraine, 54501 Vandoeuvre-lès-Nancy, France
[c] Aix-Marseille Univ., CNRS, IRD, Coll. France, UM 34 CEREGE, Technopôle de l'Environnement Arbois-Méditerranée, BP80, 13545 Aix-en-Provence, France
[d] Instituto Geológico, Minero y Metalúrgico INGEMMET, Av. Canadá 1470, Lima, Peru

ARTICLE INFO

ABSTRACT

The possibility of quantifying surface processes in mafic or volcanic environment using the potentialities offered by the *in situ*-produced cosmogenic nuclides, and more specifically by the *in situ*-produced [10]Be, is often hampered by the rarity of quartz minerals in the available lithologies. As an alternative to overcome this difficulty, we explore in this work the possibility of relying on feldspar minerals rather that on quartz to perform *in situ*-produced [10]Be measurements in such environments. Our strategy was to cross-calibrate the total production rate of [10]Be in feldspar (P_{10fsp}) against the total production rate of [3]He in pyroxene (P_{3px}) by measuring [3]He and [10]Be in cogenetic pyroxene ([3]He_{px}) and feldspar ([10]Be_{fsp}). The samples were collected from eight ignimbritic boulders, exposed from ca 120 to 600 ka at elevations ranging from 800 to 2500 m, along the preserved rock-avalanche deposits of the giant Caquilluco landslide (18°S, 70°W), Southern Peru. Along with data recently published by Blard et al. (2013a) at a close latitude (22°S) but higher elevation (ca. 4000 m), the samples yield a remarkably tight cluster of [3]He_{px} - [10]Be_{fsp} total production ratios whose weighted-mean is 35.6 ± 0.5 (1σ). The obtained weighted-mean [3]He_{px} - [10]Be_{fsp} total production ratio combined with the local [3]He_{py} total production rate in the high tropical Andes published by Martin et al. (2017) allows to establish a total SLHL [10]Be *in situ*-production rate in feldspar mineral (P_{10fsp}) of 3.57 ± 0.21 at.g^{-1}.yr^{-1} (scaled for the LSD scaling scheme, the ERA40 atm model and the VDM of Lifton, 2016).

Despite the large elevation range covered by the whole dataset (800–4300 m), no significant variation of the [3]He_{px} - [10]Be_{fsp} total production ratios in pyroxene and feldspar was evidenced. As an attempt to investigate the effect of the chemical composition of feldspar on the total [10]Be production rate, major and trace element concentrations of the studied feldspar samples were analyzed. Unfortunately, giving the low compositional variability of our dataset, this issue is still pending.

© 2017 Elsevier B.V. All rights reserved.

1. Introduction

Terrestrial Cosmogenic Nuclides (TCN) are produced through nuclear interactions between minerals of the upper Earth's crust surface and the energetic cosmic rays secondary particles. Offering the possibility to determine surface exposure durations to the cosmic ray derived secondary particles, they are useful to quantify the evolution of many geomorphological features (e.g. landslides, moraines, fault-scarps, terraces) (e.g. Gosse and Phillips, 2001). They may also provide quantitative constraints on denudation rates at a single location or at watershed scales (e.g. Brown et al., 1995; von Blanckenburg, 2005). Over the last decades, significant efforts and progress have been made not only to improve the analytical procedures (e.g. Schimmelpfennig et al., 2009; Bromley et al., 2014; Corbett et al., 2016), but also the accuracy and precision of *in situ*-production rates (e.g. Braucher et al., 2011, 2013; Fenton et al., 2011; Blard et al., 2013b; Lifton et al., 2014; Kelly et al., 2015; Martin et al., 2015; Borchers et al., 2016; Delunel et al., 2016).

In situ-produced [10]Be is one of the most commonly used TCN in quantitative geomorphology due to the fact that its production rate is relatively well constrained in the ubiquitous quartz mineral whose integrity minimizes the possibility of contamination by

* Corresponding author. Univ. Grenoble Alpes, Univ. Savoie Mont Blanc, CNRS, IRD, IFSTTAR, ISTerre, 38000 Grenoble, France.
E-mail address: swann.zerathe@ird.fr (S. Zerathe).
[1] ASTER Team: George Aumaître and Karim Keddadouche.

meteoric ^{10}Be. Easily decontaminated from meteoric ^{10}Be, it is in addition reliably measured using the Accelerator Mass Spectrometry technique for which its detection limit is lower than 10^4 at.g^{-1} (e.g. Arnold et al., 2010). However, volcanic or mafic areas are generally quartz free, which hamper the routine use of ^{10}Be. In these geological settings, other nuclide-mineral couples are used in routine, such as ^{3}He in olivine-pyroxene (e.g. Kurz, 1986), or ^{36}Cl in Ca or K rich feldspars (e.g. Schimmelpfennig et al., 2009). Nevertheless, in some cases, the applicability of these TCNs may be complicated by several limitations such as pre-exposure inheritance in the case of stable TCN (i.e. a cosmogenic component produced in an earlier exposure period) and/or large corrections for non-cosmogenic components in the case of ^{3}He (e.g. Gosse and Phillips, 2001; Blard and Farley, 2008; Amidon et al., 2009; Athanassas et al., 2016). Additionally, when production pathways are multiple such as for the ^{36}Cl, a precise knowledge of the chemical mineral composition is necessary (Phillips et al., 2001; Dunai et al., 2007) which requires measuring specific major and trace elements. Especially in the case of ^{36}Cl, despite recent important progress (Marrero et al., 2016) the problem of the scattering of the different elemental production rates in the literature (e.g. spallation from Ca and from K) is still not completely understood (see discussion in Marrero et al., 2016) and it remains a possible source of significant uncertainties.

In the case of a quartz poor lithology, an alternative possibility is to rely on ^{10}Be - feldspars. Two preliminary studies (Kober et al., 2005; Blard et al., 2013a) already provided promising results, demonstrating that the decontamination protocol classically applied to quartz (Brown et al., 1991) efficiently removes all the meteoric ^{10}Be contamination from the feldspar grains. These studies also suggest that the total production rate of ^{10}Be in feldspar is 8−10% lower than that in quartz. However, only two samples were analyzed in both studies. In order to better constrain the ^{10}Be *in situ*-production rate within feldspars, the number of samples analyzed needs to be increased. Moreover, it is important to further investigate to what extent the ^{10}Be *in situ*-production rate within feldspar depends on the chemical composition of the analyzed minerals.

In this study, we explore and demonstrate the potential of feldspar to accurately determine the concentration of in situ-produced cosmogenic ^{10}Be, thus substituting quartz in mafic areas. For this, we developed a new chemical protocol for the ^{10}Be extraction from these matrices, and to cross-calibrate the total ^{10}Be *in situ*-production rate in feldspar (P_{10fsp}) against the total ^{3}He production rate in pyroxene (P_{3px}). The cosmogenic ^{3}He and ^{10}Be concentrations were measured, respectively, in pyroxene and feldspar extracted from eight samples of ignimbrite boulders from a giant landslide located between 800 and 2500 m in the high central Andes of Southern Peru. This area is ideally located, since two studies have already determined the local total ^{3}He production rate in pyroxene on the nearby Altiplano, above 3000 m (Blard et al., 2013b; Delunel et al., 2016). Starting from the chemical protocol classically used for the extraction of the *in situ*-produced ^{10}Be from quartz, we propose a slightly updated procedure to extract the *in situ*-produced ^{10}Be from feldspar. This adapted chemical procedure allows overcoming difficulties specific to feldspars, such as the precipitation of fluorite salts during HF substitution, and also prevents from the saturation of the resin columns during cation and anion exchange chromatography.

2. Material: geomorphological and geological settings of the sampling site

The giant Caquilluco landslide is located in southern Peru (Fig. 1A), in the northern part of the Atacama Desert, about forty

kilometers north of the city of Tacna (Fig. 1B). The instability has developed along the western flank of the Peruvian Andes, an area characterized by steep slopes and extremely dry climate for the last million years (Placzek et al., 2010). A preliminary geomorphological description of this exceptional site can be found in Audin and Bechir (2006) and Crosta et al. (2015). The Caquilluco landslide is a large complex of imbricated paleo deep-seated landslides and paleo rock-avalanches. It affects the western flank of a large anticline trending NW-SE, which developed during compressive deformation propagation along west-verging blind reverse faults (e.g. the Calientes fault, Hall et al., 2012). The total volume of rock material that has been mobilized is about 15 km^3 (Crosta et al., 2015). From the head scarp (~3800 m a.s.l.) to the most distal rock-avalanche lobe (600 m a.s.l.), avalanche deposits are covering more than 40 km in distance along-strike and about 15 km in width (Fig. 1B). In the upper part of the landslide area (Fig. 1C), several rock avalanche lobes are superimposed. The relative dispositions and relationships of these lobes indicate that several successive gravitational landslides occurred and have then been preserved because of limited erosion and chemical alteration of the Atacama Desert area (e.g. Nishiizumi et al., 2005).

The Caquilluco landslide mainly remobilized Miocene ignimbrites and volcanic tuffs of the Huaylillas formation (Acosta et al., 2010). These materials, poor in quartz, are rich in feldspars and pyroxene, making these rocks suitable for cross-calibration between ^{3}He in pyroxene (^{3}He$_{px}$) and ^{10}Be in feldspar (^{10}Be$_{fsp}$). The sampling strategy was to collect samples in various landslide lobe deposits in order to cover the largest range of potential exposure durations and sampling elevations. Special care was taken to select well-preserved boulders, as large as possible (>1 m), without any apparent trace of posterior transport, significant denudation, rock fall nor desquamation (Fig. 1). A total of eight boulder samples were collected: seven (CQ1, CQ3, CQ6, CQ8, CQ10, CQ12 and CQ18; Fig. 1C) in the upper landslide zone (>2000 m a.s.l.) and one sample (TM6) on the most distal deposition area (~800 m a.s.l.; Fig. 1B). Field data and all sample characteristics are synthetized in Table 1.

In synthesis, the Caquilluco site is a good candidate for cross-calibration purpose because: (i) the landslide shows several lobes of deposits that are superimposed, which is an opportunity to span different time frames for of exposure, (ii) the area is characterized by low denudation rate and the preservation of landslide morphologies are also indicative of a good landscape preservation, and (iii) this site is the opportunity to conduct a double project: the calibration of the total ^{10}Be production rate in feldspar as well as the reconstruction of the landslide chronology to understand its failure mechanisms.

3. Methods

3.1. Sample treatment - pyroxene and feldspar separation

Thin sections were realized in each rock sample in order to ensure that enough pyroxene and feldspars were available and also to check the crystal sizes (>200 μm). Samples were then crushed, washed and sieved to select the 200−800 μm fractions. Successive magnetic separations were performed using a Frantz$^©$ magnetic separator to separate the magnetic from the non-magnetic fraction bearing pyroxene and feldspars, respectively. For efficiency, and because the magnetic fraction dominates in the ignimbrite (≥70%), the first run was done at a low magnet current (0.5−1 A) and by feeding the chute (slope of 25° and tilt 15°) with a rapid sample flow rate (≥5 g/min). This allowed a first rough separation. Then, re-running of the non-magnetic fraction was necessary to reach pure feldspars. This was done with the same chute configuration but under a slower sample flow rate (≤1 g/
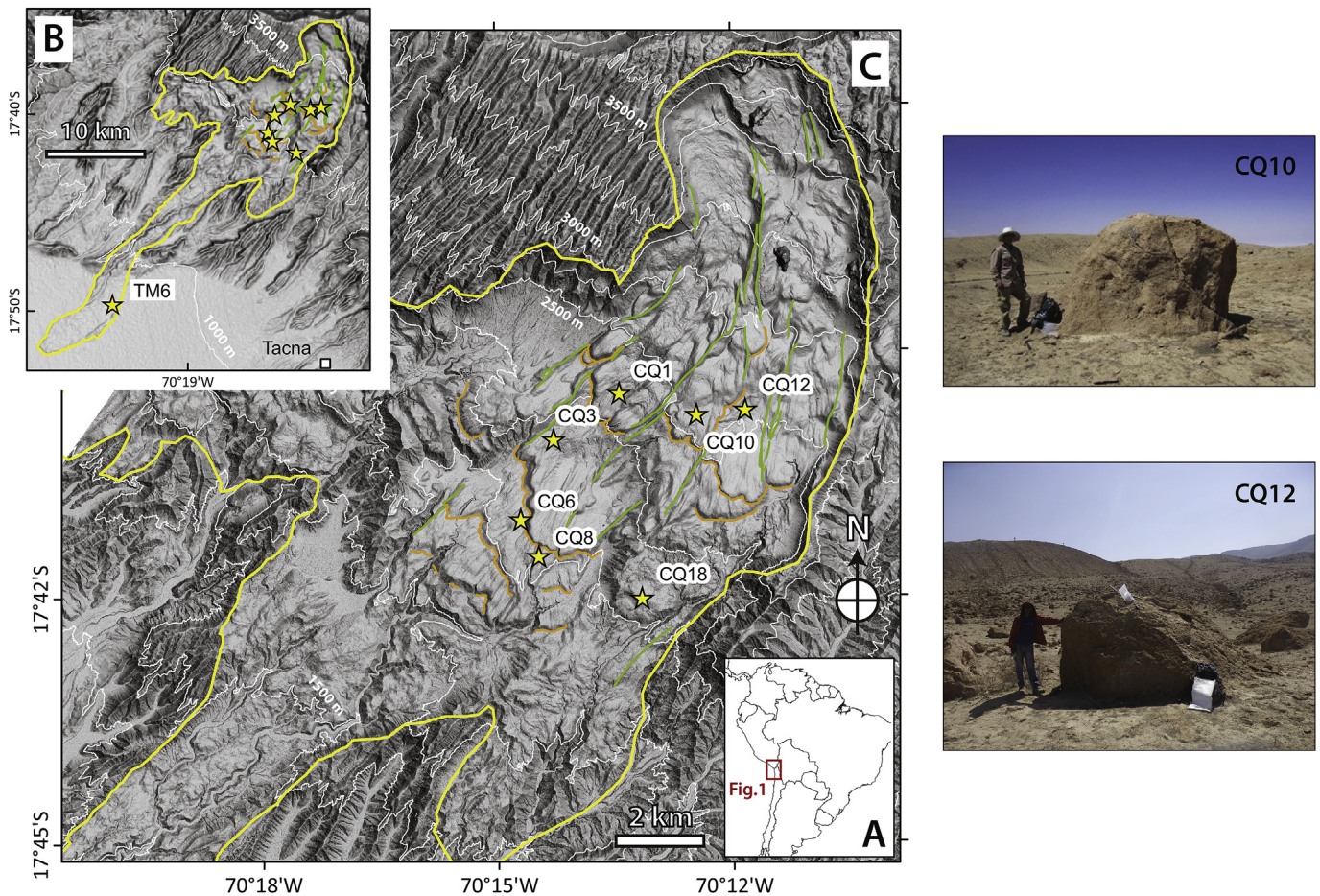
Fig. 1. Sampling site. (A) Location of the studied area in South America. (B) The giant Caquilluco landslide (surrounded in yellow) highlighted on a hillshade view computed from the ASTER DEM. Note the sample TM6 located at the landslide foot. (C) Upper part of the Caquilluco landslide and location of the seven samples "CQ". The internal structure of the landslide, showing various superimposed lobe deposits, suggests sequential rock avalanches. Lateral levees and frontal boundaries of each lobe are highlighted by green and orange lines, respectively. The two photographs on the right side show the sampled boulders CQ10 and CQ12. (For interpretation of the references to colour in this figure legend, the reader is referred to the web version of this article.)

Table 1
Sample location and field information.

Sample label	Latitude (°S)	Longitude (°W)	Elevation (m a.s.l.)	Boulder height (m)	Sample thickness (cm)	Density	Thickness correction	Shielding factor[a]
CQ1	17.65895	70.224357	2299	1.2	3.0	2.57	0.977	0.998
CQ3	17.66798	70.237950	2125	0.8	2.0	2.45	0.985	0.997
CQ6	17.68345	70.244117	2011	0.8	3.0	2.46	0.977	0.999
CQ8	17.69090	70.240383	2024	1.3	2.0	2.55	0.985	0.999
CQ10	17.66377	70.206700	2502	2.2	3.0	2.48	0.977	0.999
CQ12	17.66197	70.197162	2488	1.9	4.0	2.53	0.970	0.997
CQ18	17.70033	70.219215	2119	2.1	2.0	2.42	0.985	0.998
TM6	17.82843	70.383217	786	0.3	2.0	2.57	0.985	0.998
TU-1A[b]	19.86431	67.61281	4260	2.5	3	3	0.970	1
TU-7C[b]	19.88128	67.59733	3829	1.5	3	3	0.970	1

[a] Calculated after Dunne et al. (1999).
[b] Samples and data from Blard et al. (2013a).

min) and at a higher magnet current (~2 A). Sample purity was checked under a binocular microscope. In our case, this simple approach was efficient enough because in quartz free volcanic li-thologies, in which feldspars are the only non-magnetic fraction. However, in lithologies where the quartz content is not negligible (i.e. > 1%), other techniques may have to be applied to separate quartz and feldspar such as for example: HF-etching magnetite

approach (Iacumin and Quercioli, 1993) or the froth floatation procedure (Clifton et al., 2005).

To obtain pure pyroxenes, about 300 g of the magnetic fraction was etched in 5% hydrofluoric acid (HF) for 24 h following the procedure of Bromley et al. (2014). This method helps removing any adhering lava or mineral inclusions from the pyroxene grains and thus improves the efficiency of the magnetic separation, allowing

the recovery of 20−50% of pure pyroxene in the sample. At this stage, hand-picking under a binocular was used to isolate pure brown orthopyroxenes.

3.2. Measurement of ^{4}He and cosmogenic ^{3}He in pyroxenes

All ^{3}He and ^{4}He concentrations (^{3}He$_m$ and ^{4}He$_m$) were measured at the CRPG noble gas lab, using a Helix SFT, developed by the company GV Instruments, and following the procedures previously described in Delunel et al. (2016).

The magmatic contribution to the ^{3}He$_m$ and ^{4}He$_m$ concentrations was first estimated by a 6 min in-vacuo crushing of 40 mg of orthopyroxene of an aliquot of sample CQ10 (Kurz, 1986; Scarsi, 2000). This experiment yielded ^{3}He and ^{4}He concentrations below the detection limit, i.e. less than 10^5 and 10^{11} at.g^{-1}, respectively. Assuming that magmatic helium is quantitatively extracted by crushing, these values represent on average 1‰ of the ^{3}He concentrations and 0.5% of the ^{4}He concentrations measured by melting. This correction was thus neglected, assuming that this magmatic component is homogeneous in all the pyroxenes collected on the Caquilluco landslide, as they originate from the same ignimbrite series.

Between ca. 18 and 50 mg of pure pyroxenes of each sample were weighted and wrapped in tin foils. The samples were fused in-vacuo for 15 min at 1400 °C, using an in-house-built single vacuum furnace (Zimmermann et al., 2012). The extracted gas was purified using a succession of activated-charcoal cold traps, Ti-foam and SAES getters. Cryo-focusing of the gas at various temperatures (12 K and 70 K) allowed partial separation of helium and neon before helium analysis. It is important to note that the ^{4}He/^{20}Ne ratio was however high enough to ensure that the presence of neon does not induce an inaccurate estimate of the helium sensitivity. After the gas purification, total ^{3}He and ^{4}He concentrations were determined with the Helix SFT mass spectrometer. A re-extraction procedure was conducted on 3 samples (CQ1, CQ6 and CQ12) by heating a second time the furnace to 1400 °C for 15 min to ensure that the initial heating step was sufficient to extract all the helium from the samples. These re-extraction steps at high temperature systematically yielded blank signatures with weighted-mean values were $(1.9 ± 0.5) × 10^4$ and $(2.1 ± 0.1) × 10^9$ atoms for ^{3}He and ^{4}He, respectively. Those values represent less than 3% of the total ^{3}He extracted from the analyzed samples and less than 1% of the total ^{4}He. The SFT sensitivity was calibrated using a known amount of helium gas standard with a ^{3}He/^{4}He ratio of 20.63 Ra (1 Ra = $1.384 × 10^{-6}$ is the atmospheric ratio) (Matsuda et al., 2002). The reproducibility at the 1-sigma level on the gas standard was 1.5% for ^{3}He and 0.3% for ^{4}He over the 2-months period overlapping with our analyses (1 week). Note that a 6.0 mg aliquot of the CRONUS-P pyroxene standard was analyzed during the same analytical session and yielded a ^{3}He concentration of $(5.04 ± 0.07) × 10^9$ at.g^{-1}, in good agreement with the average value reported from an inter-laboratory comparison (Blard et al., 2015).

Potential contributions of a nucleogenic ^{3}He component (^{3}He$_n$, produced by thermal neutron capture on ^{6}Li) must be quantified for each sample (e.g. Farley et al., 2006; Amidon et al., 2009). This calculation requires the measurement of the major and trace element concentrations in the pyroxene and in the bulk rock ignimbrites, respectively (Andrews, 1985). These data were measured at the SARM-CRPG facility (Nancy, France) by ICP-OES and ICP-MS, respectively (Supp. Table 1). The age of eruption of the ignimbrites was evaluated using the (U−Th−Sm)/^{4}He method (Blard and Farley, 2008; Blard et al., 2013b). For this, the ^{4}He production rate (P$_4$) from U, Th and Sm radioactive decay was estimated for each sample from the equations of Farley et al. (2006). Corrections for α ejection and

implantation between the phenocrysts and the lava were applied (Blard and Farley, 2008). Eruption ages (t$_{eruption}$, Table 2) were then computed using:

$$t_{eruption} = {}^4He_m/P_4 \tag{1}$$

The nucleogenic ^{3}He production rate (P$_{n3}$) and its contribution (^{3}He$_n$) were finally calculated for each sample following Andrews (1985) and Andrews et al. (1982) using: 1) the (U−Th−Sm)/^{4}He eruption ages (Table 2), (2) the concentration of Li in pyroxene measured in each mineral sample by flame atomic absorption spectroscopy (Table 2), and 3) the major and trace element concentrations measured in their respective bulk rocks (Supp. Table 1).

The concentration of cosmogenic ^{3}He in the analyzed samples (^{3}He$_c$) was then corrected for the nucleogenic component:

$$^3He_c = {}^3He_m − {}^3He_n \tag{2}$$

where ^{3}He$_m$ is the concentration of ^{3}He measured when fusing the sample, ^{3}He$_n$ is the computed nucleogenic concentration. Note that we do consider here ^{3}He$_c$ as the sum of spallogenic component (induced by high-energy neutrons), the muogenic component and the component produced by capture of cosmogenic thermal neutrons (Dunai et al., 2007). As previously reported, the production by capture of cosmogenic thermal neutrons both depends on the Li content of the analyzed minerals and on the thermal neutron flux that irradiates the sampled surface (e.g. Dunai et al., 2007; Amidon and Farley, 2011).

3.3. ^{3}He exposure-age calculations

^{3}He exposure-ages were computed using the CREp program, a fully configurable and recently updated online tool (Martin et al., 2017). We applied the Lifton-Sato-Dunai (LSD) scaling model (Lifton et al., 2014) with the ERA40 atm model. Time-dependent corrections were done using the Lifton 2016 geomagnetic databases (VDM) (Lifton, 2016). The density of ignimbrites was measured by repeated weighting of each sample with different masses in pure H$_2$O at 25°, as recommended by Balco et al. (2009) for rocks of low-porosity. These densities range from 2.42 to 2.57 g.cm^{-3}, with an average value of 2.49 ± 0.06 (1σ) g.cm^{-3}. Finally, exposure ages were calculated using two different total SLHL ^{3}He production rates available in CREp: (1) the worldwide mean (WWM) value equals to 121 ± 12 at.g^{-1}.yr^{-1} (Poreda and Cerling, 1992; Cerling and Craig, 1994; Licciardi et al., 1999; Dunai and Wijbrans, 2000; Ackert et al., 2003; Blard et al., 2005, 2006;; Licciardi et al., 2006; Balco et al., 2009; Goehring et al., 2010; Amidon and Farley, 2011; Foeken et al., 2012; Blard et al., 2013b; Fenton and Niedermann, 2014; Martin et al., 2015, 2017; Delunel et al., 2016) and (2) the regional mean value for the High Tropical Andes (HTA) equals to 127.3 ± 4.6 at.g^{-1}.yr^{-1} (Blard et al., 2013b; Martin et al., 2015, 2017; Delunel et al., 2016). Note that these computed rates include both the spallation and the muonic production pathways (Martin et al., 2017). In the following, we will always refer to such total production rates except when a specific production pathway is specified.

A consequence of the hyperaridity of the Atacama Desert is that denudation rates are low (typically 1−10 mm.kyr^{-1}; Nishiizumi et al., 2005), which allows the geomorphic surfaces to survive for long periods of time, i.e. several hundred thousands of years (Kober et al., 2005; Placzek et al., 2010; Hall et al., 2012). In particular, Placzek et al. (2010) and Evenstar et al. (2009) report that boulder fields are among the most stable landforms of this area, with long-term denudation rates ranging from 0.1 to 0.2 mm.kyr^{-1}. Using the maximum boulder denudation rate from that study, we calculated

Table 2
Cosmogenic [3]He data measured on orthopyroxene.

Sample	Mass (mg)	U[a]	Th[a]	Sm[a]	Li[a]	^{4}He (10^{13} at.g^{-1})	^{3}He$_m$ (10^7 at.g^{-1})	P$_4$[b] (10^6 at.g^{-1}.yr^{-1})	(U-Th-Sm)/^{4}He eruption age (Ma)	Pn$_3$[c] (at.g^{-1}.yr^{-1})	^{3}He$_n$ (10^6 at.g^{-1})	% ^{3}He$_n$/^{3}He$_t$	^{3}He$_c$[d] (10^7 at.g^{-1})
CQ1	18.70	<LD.	0.40	0.89	16.1	2.45 ± 0.07	5.43 ± 0.22	1.72 ± 0.27	14 ± 6	0.096	1.34 ± 0.21	2.5	5.30 ± 0.24
CQ3	15.80	<LD.	0.38	0.27	14.7	1.68 ± 0.05	4.55 ± 0.20	1.59 ± 0.25	11 ± 4	0.081	0.85 ± 0.13	1.9	4.47 ± 0.21
CQ6	41.30	<LD.	0.62	1.17	14.8	2.29 ± 0.06	9.66 ± 0.18	1.88 ± 0.27	12 ± 4	0.086	1.04 ± 0.15	1.1	9.56 ± 0.20
CQ8	50.20	<LD.	0.40	0.48	16.7	2.16 ± 0.06	11.27 ± 0.19	2.14 ± 0.36	10 ± 4	0.112	1.12 ± 0.19	1.0	11.16 ± 0.21
CQ10	30.50	0.06	0.44	0.71	17.1	2.65 ± 0.07	6.56 ± 0.15	1.80 ± 0.25	15 ± 5	0.095	1.43 ± 0.20	2.2	6.41 ± 0.17
CQ12	19.00	<LD.	0.49	0.55	9.3	2.89 ± 0.08	15.35 ± 0.31	1.74 ± 0.26	17 ± 6	0.054	0.92 ± 0.14	0.6	15.26 ± 0.32
CQ18	39.80	0.07	0.403	1.01	15.4	1.36 ± 0.04	18.28 ± 0.28	1.68 ± 0.23	8 ± 3	0.077	0.61 ± 0.08	0.3	18.21 ± 0.29
TM6	30.70	0.15	0.52	0.64	14.9	3.94 ± 0.10	8.35 ± 0.18	2.42 ± 0.30	16 ± 5	0.083	1.33 ± 0.17	1.6	8.22 ± 0.20
TU-1A*	62.2	–	–	–	15	0.35 ± 0.01	2.00 ± 0.06	–	1.2 ± 0.3	–	0.19 ± 0.06	0.9	1.96 ± 0.06
TU7C*	35.1	–	–	–	31	0.3 ± 0.01	20.18 ± 0.49	–	1.2 ± 0.3	–	0.39 ± 0.12	0.2	20.10 ± 0.48

* Samples and data from Blard et al. (2013b), not corrected for sample thickness.

  [a] Concentrations in ppm measured in the orthopyroxene. Measurements were done by ICP-MS at the SARM-CRPG facility (Nancy, France). Uncertainties are below 10% and correspond to the mean deviation deduced from several routine analyses on geostandards (for more information please see http://helium.crpg.cnrs-nancy.fr/SARM/pages/geostandards.html#). <LD. stands for "not detectable".

  [b] Radiogenic ^{4}He production rate (P$_4$) calculated using equations of Farley et al. (2006), the U, Th and Sm content measured in both pyroxene phenocrysts (this table) and bulk rock (see supp. Table 1) and assuming a mean phenocryst radius of 100 ± 20 μm, which was evaluated under a binocular microscope.

  [c] Nucleogenic ^{3}He production rate (P$_{n3}$) Calculated using the equations of Andrews (1985) and Andrews et al. (1982), the Li content of pyroxene (this table) and major and trace element composition of the bulk rock (supp. Table 1).

  [d] Corrected ^{3}He concentration (^{3}He$_c$) obtained after subtracting the nucleogenic ^{3}He component (^{3}He$_n$) from the total measured ^{3}He component (^{3}He$_m$). The magmatic component was neglected, as a 6 min crushing experiment of sample CQ10 yielded a ^{3}He concentration lower than 10^5 at.g^{-1} and a ^{4}He concentration lower than 10^{11} at.g^{-1}.

the exposure ages using a denudation rate of 0.2 mm.kyr^{-1}. We assume that these exposure ages can be considered as maximum ages based on the following assumptions: (i) the 0.2 mm.kyr^{-1} is the maximum denudation rate, (ii) the surface of deposits have never been covered and (iii) the boulders have not been toppled. Exposure-ages without denudation correction are also provided in the Supplementary Data file. Considering no denudation, the determined exposure durations are about 2–5% younger than those calculated considering a 0.2 mm.kyr^{-1} denudation rate. The difference reaches ca. 10% for the two oldest samples (CQ18 and TM6). The synthetic data templates for further inputs in the CREp calculator are available in the Supplementary Data file.

3.4. Measurement of cosmogenic [10]Be in feldspars

3.4.1. Extraction of [10]Be from feldspars

To extract the *in situ*-produced [10]Be from feldspars, the routinely used chemical protocol used for quartz was adjusted to take into account the high cationic content of feldspars yielding to fluorides after addition of HF. Similarly to what is performed for quartz samples, to get rid of the [10]Be meteoric contamination, three sequential HF dissolutions were performed, each step dissolving ~10% of feldspars (Kober et al., 2005; Blard et al., 2013a). Note that if considering quartz minerals about 4 ml of 40% HF are required to dissolve ~1 g of SiO$_2$, only ~2 ml are required while considering feldspars. Once pure feldspars were obtained, a few grams were sent to the SARM (Nancy) for major and trace analyses (Supplementary data). For any major and trace analyses, for instance in order to determine the concentration of native [9]Be in the mineral, we highly recommend to split the sample after HF leaching and to use a rotary sample splitter to obtain representative samples.

After the addition of 100 ml of a concentrated [9]Be carrier solution (3.025 ± 0.009 × 10^{-3} g [9]Be/g (Merchel et al., 2008)), about 10 g of feldspar were totally dissolved. This mass limitation is due to the fact that feldspars, when they are dissolved in highly concentrated HF, form a subsequent precipitation of colloids, even at very low pH value (<1). These colloids are composed of a mixture of several species of fluoride-based minerals (e.g. AlF$_3$, CaF$_2$, NaF), (Al-harbi et al., 2012). If directly evaporated and substituted by HCl solution as it is the case for pure quartz, these fluorite salts may produce massive precipitates in the Teflon beaker. These solid salts may not

only hamper a proper pipetting of the solution containing the beryllium but also may trap beryllium yielding to a massive loss of this element. We therefore highly advise, before evaporation, to remove the resulting colloids by centrifugation. To prove that the beryllium is correctly retrieved without significant fractionation or mass loss, it has been verified that the colloids do not hold a significant amount of beryllium. This has been done on ~300 mg colloid aliquots resulting from the dissolution of samples CQ1 and CQ3. Measurements were performed by ICP-MS at ISTerre (Grenoble, France) using a Thermo X serie2 ICP-MS. The aliquots were dehydrated (24 h at 150 °C) to quantify their water content (>90%), then, dry residues were weighed and dissolved using high-purity grade 14N HNO$_3$. After evaporation, the residues were dissolved in 2% HNO$_3$ with traces of HF to obtain a dilute solution. The ICP-MS calibration was established using several pure beryllium solutions (Scharlab ICP Standard) (from 100 ppt to 50 ppb) and the addition of 50 ppb of indium as internal standard. The obtained results show that the beryllium contents in the gels resulting from the dissolution of samples CQ1 and CQ3 are 0.14 and 0.16 ppm, respectively, much less than the amount added through the [9]Be spike.

Once centrifuged, the supernatant solutions were evaporated and beryllium extraction was done as for quartz using anionic and cationic resins. It is important to mention that depending on the aluminum content of each sample, extraction in cationic column chromatography had to be repeated (from one to 6 times) to remove the major part of Al. To evaluate if additional resin extraction steps were required, we visually compared the volume of the Be gel of the sample with the one of the blank as a reference. If the volume of the Be gel was at least more than 2 times larger than the blank one, some additional cycles of cationic column chromatography were performed. In our case, this simple approach was ample enough to reach high-purity Be fractions, as confirmed by the high quality of the final BeO targets analyzed at the Accelerator Mass Spectrometry (AMS) facility (high and stable [9]Be beam currents leading to uncertainty of [10]Be/[9]Be ratios of ~3%, Table 4). As described for quartz in Corbett et al. (2016), a possibility to optimize ion exchange chromatography methods is to remove replicate aliquots at the end of the extraction process and before beryllium hydroxide precipitation. ICP-OES measurements of Be, Al, B and Ti fractions on these aliquots will allow to check the procedure yield and the sample purity. Knowing the concentrations of the remaining undesirable ions will eventually help to properly size the

ion exchange column chromatography and enhance the sample purity (see discussion in Corbett et al., 2016).

Finally, beryllium oxy-hydroxides precipitated by increasing the pH to 8 using an ammonia solution were oxidized at 800° for one hour. The obtained BeO was then mixed with niobium powder and measured by AMS.

3.4.2. ^{10}Be measurements

^{10}Be measurements were carried out at the French National AMS facility ASTER (Arnold et al., 2010, 2013) located at the CEREGE laboratory (Aix-en-Provence). The ^{10}Be/^{9}Be ratios were calibrated against NIST Standard Reference Material 4325 with an assigned ^{10}Be/^{9}Be ratio of 2.79×10^{-11} (Nishiizumi et al., 2007), corresponding to a ^{10}Be half-life of $1.387 \pm 0.012 \times 10^6$ yrs (Korschinek et al., 2010; Chmeleff et al., 2010). Analytical uncertainties include the counting statistics, the machine stability (~0.5%, Arnold et al., 2010) and the blank correction whose ^{10}Be/^{9}Be value was $2.93 \pm 0.45 \times 10^{-15}$ during the concerned measurement run.

4. Results

4.1. Helium isotopic results

4.1.1. (U−Th−Sm)/^4He ages and nucleogenic ^3He correction

Helium isotopic data and derived calculation results related to this paragraph are presented in Table 2. The major and trace element concentrations measured both in the pyroxene phenocrysts and in the bulk ignimbrite are available in the Supplementary Material file (Supp. Table 1). The 8 obtained (U−Th−Sm)/^{4}He pyroxene crystallization ages range between 8 ± 3 and 17 ± 6 Ma. It is worth noting that these ages should be considered as minimum ages because: (i) as the pyroxene were etched, an unknown fraction of the surface layer containing the ^{4}He component injected from the matrix may have been lost, and (ii) some radiogenic ^{4}He may have been diffused out of the pyroxene since the millions of years since their crystallization. Nevertheless, these eruption ages are in relatively good agreement with the previous Ar-Ar time constraints obtained in that region (Quang et al., 2005). Indeed, all these ignimbrite samples remobilized by the Caquilluco landslide (Fig. 1) initially originate from the thick (ca. 500 m thickness) Huaylillas Formation (Acosta et al., 2010). The Huaylillas ignimbrite series were deposited during various volcanic eruption phases lasting between 10.1 and 19.1 Ma (Ar-Ar dating from Tosdal et al. (1981), Quang et al. (2005) and references therein). The maximum

eruption age for these ignimbrites is therefore ca. 19 Ma (Quang et al., 2005) and the scatter of the determined crystallization ages suggests that the sampled boulders may originate from different levels in the ignimbrite series corresponding to different episodes of ignimbrite eruptions. The nucleogenic ^{3}He production rates (P_{n3}) calculated for each sample range from 0.05 to 0.1 at.g^{-1}.yr^{-1}. Combined with the (U−Th−Sm)/^{4}He eruption ages, this allows the calculation of the nucleogenic ^{3}He contribution for each sample (^{3}He$_n$) which ranges from $0.61 \pm 0.08 \times 10^6$ to $1.43 \pm 20 \times 10^6$ at.g^{-1}. On average, the ^{3}He$_n$ contribution represents 1.5% of the total ^{3}He concentration measured by fusion of phenocrysts (^{3}He$_m$). This falls within the global analytical uncertainties of ^{3}He mass spectrometry measurements (ca. 1.5%), indicating that the nucleogenic ^{3}He correction is not a significant source of uncertainty in this dataset. Note that even considering a maximum eruption age of 19 Ma for the Huaylillas ignimbrite (Quang et al., 2005), the ^{3}He$_n$ contribution would still be lower than 3%.

The corrected ^{3}He concentrations (^{3}He$_c$) range from $2.02 \pm 0.06 \times 10^7$ to $18.21 \pm 0.29 \times 10^7$ at.g^{-1} (Table 2).

4.1.2. ^3He exposure-ages

^{3}He exposure age results are presented in Table 3. Exposure ages from the Caquilluco landslide range from 118 ± 11 to 627 ± 66 ka and from 112 ± 6 to 590 ± 26 ka (1σ external uncertainty) using the WWM production rate (121 ± 12 at.g^{-1}.yr^{-1}, Borchers et al., 2016) and the HTA production rate (127.3 ± 4.6 at.g^{-1}.yr^{-1}, Martin et al., 2015, 2017), respectively. Exposure ages from the Tunupa volcano, recalculated from Blard et al. (2013b), lead to 17 ± 2 and 182 ± 14 ka, and 16 ± 1 and 174 ± 7 ka for the WWM and the HTA production rates, respectively.

4.2. Cosmogenic ^{10}Be concentrations in feldspars

^{10}Be concentrations measured in feldspars are ranging from $1.17 \pm 0.03 \times 10^6$ to $5.06 \pm 0.15 \times 10^6$ at.g^{-1} (Table 4). It is important to note that trace element measurements performed on pure feldspars have revealed a significant content of native ^{9}Be in our samples (~1.5 ppm, Supplementary data). Considering the mass of sample dissolved, the native ^{9}Be content represents between 3 and 6% of the ^{9}Be carrier added as a spike (Table 4) and this correction was taken into account in the calculations of ^{10}Be concentrations. If the contribution of native ^{9}Be had been neglected in our study, the ^{10}Be concentrations in feldspars would have been underestimated by 3−5%. To our knowledge, the possible range of ^{9}Be concentration

Table 3
^{3}He exposure-ages calculated using the online CREp calculator (Martin et al., 2017). The scaling scheme LSD (Lifton et al., 2014) is applied in concert with the VDM geomagnetic database for the geomagnetic correction (Lifton, 2016), and the ERA40 atm model (Uppala et al., 2005). Two ^{3}He total SLHL production rates are considered: (i) the world wide mean value (121 ± 12 at.g^{-1}.yr^{-1}; Phillips et al., 2016) and (ii) the mean value obtained for the high tropical Andes (127.3 ± 4.6 at.g^{-1}.yr^{-1}; Martin et al., 2015, 2017; Delunel et al., 2016). These ages are corrected for denudation, assuming an average denudation rate of 0.2 mm.kyr^{-1} (Evenstar et al., 2009; Placzek et al., 2010). As an indication, exposure-ages calculated with no denudation are available in supplementary data. Scaling factors are mean values integrated over the exposure duration.

Sample	Worldwide mean ^{3}He production rate (121 ± 12 at.g^{-1}.yr^{-1})				High tropical Andes ^{3}He production rate (127.3 ± 4.6 at.g^{-1}.yr^{-1})			
	Scaling factor	Age (ka)	Internal uncert. (1σ)	External uncert. (1σ)	Scaling factor	Age (ka)	Internal uncert. (1σ)	External uncert. (1σ)
CQ1	3.65	124	5	12	3.64	118	4	6
CQ3	3.21	118	5	11	3.21	112	5	6
CQ6	2.98	272	5	25	3.00	258	5	11
CQ8	3.02	312	6	29	3.04	295	5	11
CQ10	4.19	130	3	12	4.21	124	3	5
CQ12	4.14	316	7	31	4.18	299	6	11
CQ18	3.02	510	8	46	3.04	481	8	20
TM6	1.11	627	17	66	1.12	590	14	26
TU-1A*	10.21	16.9	0.5	1.5	10.16	16.1	0.4	0.7
TU-7C*	9.68	182	3	14	9.61	174	4	7

* Data from Blard et al. (2013b) recalculated for internal consistency.

Table 4
Cosmogenic ^{10}Be data measured on feldspar and derived individual R$_{3/10}$ (measured ^{3}He$_{px}$ - ^{10}Be$_{fsp}$ ratios) and P$_{3/10}$ (^{3}He$_{px}$ - ^{10}Be$_{fsp}$ production ratios) values. P$_{3/10}$ ratios are calculated considering two different total ^{3}He production rates: the worldwide mean value (WWWM P$_3$) and the high tropical Andes mean value (HTA P$_3$).

Sample	Mass (g)	^{9}Be carrier (10^{19} atoms)	Native ^{9}Be[a] (10^{19} atoms)	Total ^{10}Be counts	^{10}Be/^{9}Be ratio (10^{-13})	^{10}Be[b] (10^6 at.g^{-1})	Measured ^{3}He$_{px}$/^{10}Be$_{fsp}$ ratios	Production ratios[c,e] WWM P$_{3/10}$	Production ratios[d,e] HTA P$_{3/10}$
CQ1	10.011	2.005	0.105	1234	5.55 ± 0.18	1.17 ± 0.03	45.3 ± 2.4	45.1 ± 4.7	45.4 ± 2.5
CQ3	5.413	2.001	0.055	1190	3.42 ± 0.11	1.30 ± 0.04	34.4 ± 1.9	34.0 ± 3.6	34.3 ± 1.9
CQ6	8.994	2.030	0.091	869	10.57 ± 0.41	2.49 ± 0.08	38.3 ± 1.5	36.7 ± 3.9	37.1 ± 2.2
CQ8	10.210	2.013	0.106	1239	14.70 ± 0.45	3.05 ± 0.09	36.6 ± 1.3	34.4 ± 3.7	34.8 ± 2.0
CQ10	7.649	2.033	0.076	802	5.34 ± 0.21	1.47 ± 0.05	43.6 ± 1.9	43.3 ± 4.4	43.6 ± 2.2
CQ12	8.696	2.032	0.090	1223	16.15 ± 0.53	3.94 ± 0.11	38.7 ± 1.4	37.0 ± 4.2	37.5 ± 2.6
CQ18	10.744	2.034	0.113	1152	25.35 ± 0.88	5.06 ± 0.15	36.0 ± 1.2	32.3 ± 4.0	32.7 ± 2.7
TM6	10.045	2.017	0.100	1240	9.32 ± 0.29	1.96 ± 0.06	41.8 ± 1.6	36.7 ± 3.8	37.1 ± 1.9
TU-1A*	–	–	–	–	–	–	33.7 ± 7.5	34.5 ± 4.1	34.5 ± 2.7
TU-7C*	–	–	–	–	–	–	37.5 ± 1.4	36.9 ± 4.6	36.9 ± 3.3

* Data from Blard et al. (2013a) recalculated for internal consistency.
  [a] Calculated on the basis of Be measurements available in Supplementary material.
  [b] Analytical uncertainties are 1σ and include the counting statistics, the machine stability (~0.5%) and the blank correction whose obtained ^{10}Be/^{9}Be ratio was (2.9 ± 0.4) x 10^{-15} for this session.
  [c] P$_{3/10}$ ratios calculated taking into account the total worldwide mean ^{3}He production rate (WWM P$_3$: 121 ± 12 at.g^{-1}.yr^{-1}).
  [d] P$_{3/10}$ ratios calculated taking into account the total high tropical Andes mean ^{3}He production rate (HTA P$_3$: 127.3 ± 4.6 at.g^{-1}.yr^{-1}).
  [e] Analytical uncertainties are 1σ and include the propagation of the uncertainty of each parameter in Equation (3).

in feldspar minerals remains mostly unknown. However, previous studies such as Portenga et al. (2015) have already detected ^{9}Be in purified quartz at levels up to tens of ppm. Therefore, and in any case, those results point out the importance of measuring the native ^{9}Be content of mineral target for any cosmogenic ^{10}Be applications.

5. Discussion

5.1. ^{3}He$_{px}$ - ^{10}Be$_{fsp}$ production ratios

The ten ^{3}He$_{px}$ - ^{10}Be$_{fsp}$ concentration couple values, measured respectively in co-genetic pyroxene and feldspar, include eight samples from boulders of the Caquilluco landslide (this study) and two samples from boulders of the Tunupa volcano (Blard et al., 2013a). Their distribution in a plot of ^{3}He versus ^{10}Be nuclide concentrations are highly linearly correlated (R^2 = 0.99) as highlighted on Fig. 2. This indicates that, at the first order, the concentrations of ^{3}He in pyroxene and ^{10}Be in feldspar were accumulated in the same relative proportions over the timespan covered by our dataset (ca. 600 ka) and that the production rate of ^{10}Be in feldspar is constant from one sample to another. Moreover, this linear correlation also indicates that, at the first order, neither potential inheritance, nor differential denudation, should be a significant source of uncertainties.

The ten measured ^{3}He$_{px}$/^{10}Be$_{fsp}$ concentration ratios (R$_{3/10}$) vary from 33.7 ± 7.5 to 45.3 ± 2.4 (Table 4). In order to convert the measured R$_{3/10}$ concentration ratios into ^{3}He$_{px}$ - ^{10}Be$_{fsp}$ production ratios (P$_{3/10}$), a correction taking into account the exposure duration is required (Blard et al., 2013a). Indeed, while the ^{3}He is a stable TCN, the ^{10}Be TCN is radioactive and decays with a half-life of 1.387 ± 0.012 × 10^6 yrs (Korschinek et al., 2010; Chmeleff et al., 2010). To take into account the ^{10}Be radioactive decay that occurred since the beginning of the TCN production (i.e. the beginning of sample exposure), the P$_{3/10}$ production ratio calculations were done using the equation of Blard et al. (2013a) derived from the equation of Lal (1991):

$$P_{3/10} = \frac{f * P_3}{\lambda_{10} * ^{10}Be} \times \left(1 - e^{-\lambda_{10}*t}\right) \qquad (3)$$

where f is the geographic and time-dependent scaling factor of the total production rate (derived from the CREp outputs, Table 3), λ$_{10}$

(yr^{-1}) is the ^{10}Be radioactive decay constant, P$_3$ is an independently constrained total SLHL ^{3}He production rate (at.g^{-1}.yr^{-1}) and t is the ^{3}He exposure-age calculated using CREp (Table 3). For each sample, we calculated two variants of the P$_{3/10}$ ratio applying two different of total SLHL ^{3}He production rates: (1) the WWM production rate (121 ± 12 at.g^{-1}.yr^{-1}, Borchers et al., 2016) and (2) the HTA production rate (127.3 ± 4.6 at.g^{-1}.yr^{-1}, Martin et al., 2015, 2017), as well as their f and t associated values (Tables 3 and 4).

The so-corrected P$_{3/10}$ ratios range from 34.5 ± 4.2 to 45.1 ± 4.7 and from 34.5 ± 2.7 to 45.4 ± 2.5 for the WWM and the HTA total SLHL ^{3}He production rates, respectively. A chi-square test considering the 95% level of confidence ($\chi^2_{(95\%)}$) (Ward and Wilson, 1978) reveals that two samples, CQ1 and CQ10, are statistical outliers. The same conclusion can be reached through the graphical analysis of a probability density plot (Fig. 3), also showing that CQ1 and CQ10 are outliers, while the rest of the dataset display a unimodal distribution. Discarding those two samples, the obtained weighted-means are 35.2 ± 1.4 ($\chi^2_{(95\%)}$=1.32/14.07) and 35.6 ± 0.8 ($\chi^2_{(95\%)}$=3.62/14.07) for the WWM and the HTA total SLHL ^{3}He production rates, respectively. The MSWD (mean squares of the weighted deviates; McIntyre et al., 1966) of these two datasets are 0.5 and 0.2, respectively. These values are lower than one, also indicating the absence of remaining outliers and a good agreement between the observed scatter and the calculated analytical errors.

The two anomalously high P$_{3/10}$ values obtained for CQ1 and CQ10 can most likely be explained by an excess of ^{3}He in those samples, the concentration of which may be inherited from a previous exposure history. Indeed, the Miocene ignimbrite series providing the landslide materials have been deposited in terrestrial conditions, during large episodes of strato volcanoes activities along the West Andean flank (e.g. Wörner et al., 2002). It is therefore plausible that, between successive eruption phases, depositional surfaces of ignimbrites were exposed to cosmic ray irradiation for a few thousands of years. This would have led to TCN production and accumulation (e.g. both ^{10}Be and ^{3}He) in the mineral lattice of ignimbrites over the first meters below the surface. Then, when the surfaces were covered by the subsequent volcanic series, the TCN productions stopped and, while the ^{10}Be content started to decrease by radioactive decay, the stable ^{3}He remained constant. Thus, when those rocks were remobilized by landsliding after several million years of burial (cf. Table 2), more than 90% of the initial ^{10}Be concentration in feldspar must have disappeared
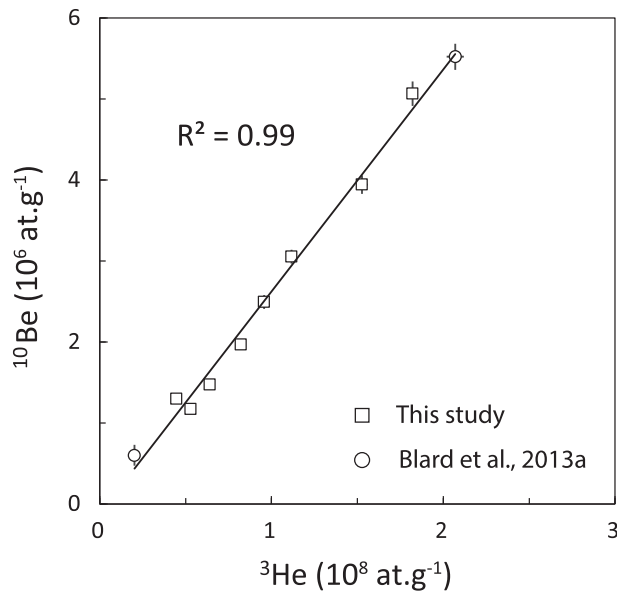
Fig. 2. Concentrations of ^{3}He versus ^{10}Be measured in co-genetic pyroxene and feldspar, respectively. Associated uncertainties are reported even if they may be smaller than the point for some samples.

(Gosse and Phillips, 2001) but the inherited ^{3}He can be still present in pyroxene.

To examine the robustness of the hypothesis that ^{3}He is in excess in the CQ1 and CQ10 samples, the measured cosmogenic nuclide concentrations were plotted in a "two-nuclides" diagram (sometimes called "banana plot") presenting the evolution of the theoretical $R_{3/10}$ values as a function of the ^{3}He concentrations

Fig. 3. Probability density plot of the ^{3}He$_{px}$ - ^{10}Be$_{fsp}$ production ratios (P$_{3/10}$) calculated for the HTA total SLHL ^{3}He production rate. The red dashed curve is a Gaussian fit of the summed probability density function (pdf). The data set includes eight samples from this study and two samples from Blard et al. (2013a). Results of their statistical analysis are reported. (For interpretation of the references to colour in this figure legend, the reader is referred to the web version of this article.)

(Fig. 4). The $R_{3/10}$ versus ^{3}He concentration curves showed Fig. 4 were calculated for a mean elevation at 2500 m a.s.l. considering, respectively, "steady-state denudation" and "no denudation". The HTA ^{3}He production rate in pyroxene (Martin et al., 2017 and references therein) and the ^{3}He$_{px}$ - ^{10}Be$_{fsp}$ production ratios derived from this study (Fig. 3) were used. Taking into account the ±1 sigma uncertainties associated to the scaling factors and the production rates, three areas can be distinguished (Fig. 4): a "simple exposure area" in between the ±1 sigma curves (gray area), a "burial area" on the left below the −1 sigma curve, and a "forbidden area" on the right above the +1 sigma curve. Most of the samples belong to the "simple exposure area", while the two, CQ1 and CQ10 tow samples belong to the "burial area", suggesting a long pre-burial duration before their final surface exposure. Finally, the ^{10}Be$_{fsp}$ concentration of the boulder CQ2, located a few hundred meters away from CQ1, and in the same lobe deposit (not included in our ^{3}He analysis because the macroscopic observations did not indicate significant amount of pyroxene in this rock), is $1.09 \pm 0.06 \times 10^6$ at.g^{-1} (taking into account sample thickness correction). This concentration is indistinguishable from the one of CQ1 ($1.14 \pm 0.03 \times 10^6$ at.g^{-1}, taking into account sample thickness correction), which also supports the hypothesis of ^{3}He excess in the sample CQ1.

The possible variation of production ratios of different TCNs with altitude has been the matter of an important debate (e.g. Gayer et al., 2004; Amidon et al., 2008; Schimmelpfennig et al., 2011; Argento et al., 2013; Blard et al., 2013a; Delunel et al., 2016). If real, such an altitude dependence of production ratios might imply that nuclide-specific scaling factors would become necessary. Up to now, in the case of P$_{3/10}$, some modeling studies (e.g. Argento et al., 2013) have suggested an increase of a few percent of the P$_{3/10}$ between sea-level and 5000 m, but this still remains undemonstrated by the most recently updated global dataset (Blard et al., 2013a). Added to the two data (TU-1A and TU-7C) of Blard et al. (2013a), samples from the giant Caquilluco landslide provide a new P$_{3/10}$ cross calibration elevation transect in the central Andes. Despite covering a large altitude range from ca. 800 m−4300 m, the presented dataset does not show any tendency with elevation (Fig. 5) and these eight P$_{3/10}$ individual production ratios are not significantly different. Therefore, our contribution does also agree with the assumption that atmospheric attenuations are similar for ^{10}Be and ^{3}He, without further need of nuclide-specific scaling factors (Blard et al., 2013b; Schimmelpfennig et al., 2011).

5.2. ^{3}He$_{px}$ - ^{10}Be$_{fsp}$ production ratios and the chemical composition of feldspar

At the Earth's surface, ^{10}Be is mainly produced in minerals through spallation reactions on O and to a lesser extent on heavier elements such as Si, Mg, Al, Ca and trace elements (Gosse and Phillips, 2001; Masarik et al., 2007; Kober et al., 2005; Dunai, 2010). While quartz is characterized by a unique and simple molecular structure (SiO$_2$), feldspar minerals present a large diversity of chemical compositions from potassium-feldspar (KAlSi$_3$O$_8$) to plagioclase-feldspar (NaAlSi$_3$O$_8$ - CaAl$_2$Si$_2$O$_8$). We may therefore wonder to what extent this composition variability impacts the P$_{10fsp}$. From a theoretical point of view, we suggest that the ^{10}Be production rate in feldspar minerals would not be very sensitive to their elemental compositions (Masarik, 2002; Kober et al., 2005). First, O, that is the dominant target, is the main molecular component of feldspars and its relative abundance does not significantly vary between different feldspar species (theoretically 8 atoms per molecule). Second, spallation reactions on other elements such as Si, Al, Ca or Na were found to lead to specific ^{10}Be production rates about 2−6 times lower than that resulting from
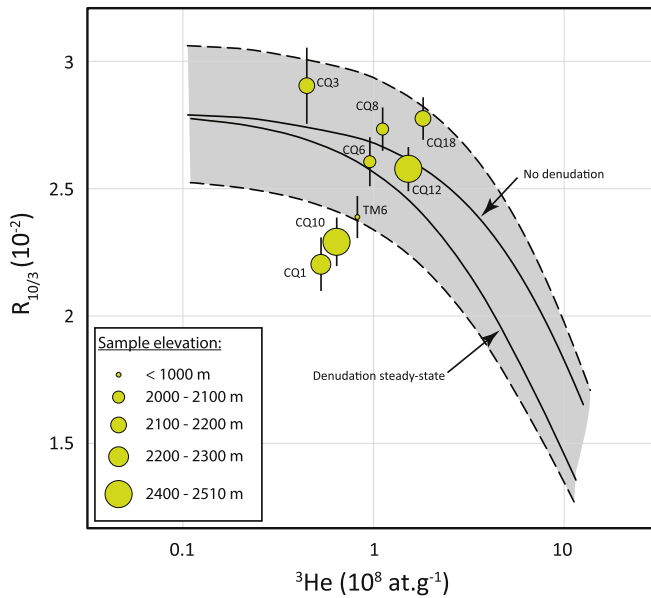
Fig. 4. Two-nuclides plot showing theoretical relations between $R_{3/10}$ values and ^{3}He concentrations for a mean scaling at 2500m a.s.l. taking into account a steady-state denudation (lower black curve) and no denudation. Dashed lines correspond to the propagation of one sigma of uncertainty. Both theoretical ^{3}He concentration and $R_{10/3}$ value were calculated considering the weighted-mean $P_{3/10}$ (35.6 ± 0.8, Fig. 3) and the $P_3 = 127.3 ± 4.6$ at.g^{-1}.yr^{-1} (Martin et al., 2017). The gray field between the curves corresponds to the "simple exposure area" whereas outside to the curves lie the "forbidden area" and "the burial area" i.e. suggesting an excess of ^{10}Be or ^{3}He when samples are located above or below the gray field, respectively. Samples CQ1 and CQ10 lie in the lower "burial area" and thus exhibit an excess of ^{3}He. Specific attention may be paid to TM6 whose elevation range is significantly lower than others (786 m a.s.l., Table 1). Taking into an appropriate scaling at ca. 800 m a.s.l., this point also correctly belongs to the "simple exposure area".
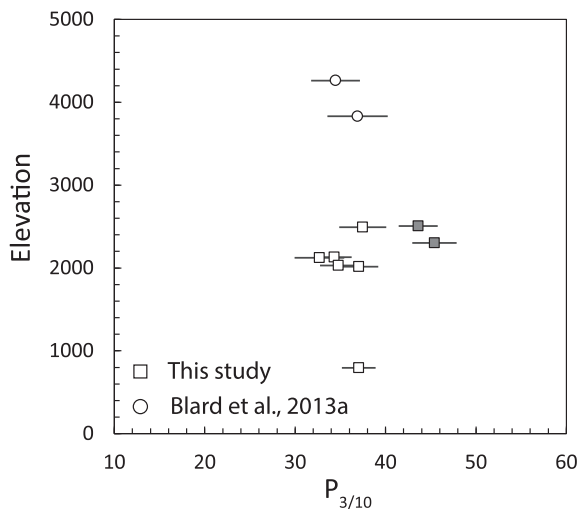

Fig. 5. $P_{3/10}$ production ratios (calculated for the HTA ^{3}He production rate) versus sample elevations. The two grayed samples are the outliers CQ1 and CQ10.

spallation reactions on O (Masarik, 2002; Kober et al., 2005). Considering two different feldspar varieties such as for instance Albite (NaAlSi$_3$O$_8$) and Microcline (KAlSi$_3$O$_8$), we suggest therefore that interchanges between K and Na in the molecular structure will not affect the production rate determined for the mineral species beyond analytical uncertainties of ^{10}Be measurements, i.e. to more than a few percents.

As an attempt to further investigate this question, we measured

the chemical composition of the 8 studied feldspar samples (Section 3.4.). Raw major and trace element compositions are available in the Supplementary Data file. In Table 5, we present major chemical compositions that were normalized such that the sum of all oxides equals 100% for each sample neglecting the relative effect of the variation of the lost on ignition. These results show (1) a low compositional variability between all samples, the standard deviation being below 1% for each oxide, (2) a negligible content in K and Fe, and (3) a mean composition corresponding to Andesine feldspars (recalculated mean mineral formula being ca. Na$_{0.6}$Ca$_{0.4}$Al$_{1.3}$Si$_{2.7}$O$_8$).

Tentative correlations between $P_{3/10}$ values and cation content of the mineral targets are presented in Fig. 6. Unfortunately, it must be recognized that given the almost complete lack of compositional variation in the samples that were processed for this study, it is not possible to do more than hypothesize on the lack of compositional dependence based on this particular data set. This issue must be address in the future, rigorously selecting a variety of feldspar as large as possible.

The obtained $P_{3/10}$ production ratios are not correlated with the Li content of the analyzed pyroxenes (Li ranges from 8 to 32 ppm), suggesting that the production by capture of cosmogenic thermal neutrons is not detectable in these samples (Fig. 7). Such low sensitivity was already observed in a recent study that cross-calibrated the total production rate of ^{3}He in pyroxenes with the one of ^{10}Be in quartz (Blard et al., 2013b).

5.3. ^{10}Be production rate in feldspar

Final estimates of P_{10fsp} are presented in Table 6. They were obtained by combining the weighted-average of $P_{3/10}$ ratios with total SLHL ^{3}He pyroxene production rates. Note that these computed rates include both the spallation and the muonic production pathways. Two P_{3px} were used: (1) the most recently updated worldwide average and (2) the regional average corresponding to the study area, i.e. the high tropical Andes. Following recommendations of Martin et al. (2017), those two P_{3px} were computed according to each combination of scaling schemes, atmosphere models, and geomagnetic database implemented in the CREp online calculator. Future ^{10}Be - feldspar users will thus be able to load the appropriate SLHL P_{10fsp} corresponding to the specific parametrization of CREp they want to use (see Appendix 2 in Martin et al., 2017). It is however beyond the scope of this paper to discuss the advantages/limitations of the different scaling schemes and parametrizations that are available in CREp. Many discussions on those topics could be found for instance in Lifton et al. (2014), Borchers et al. (2016), Delunel et al. (2016), Phillips et al. (2016), Martin et al. (2017).

Applying the most recent parametrization in CREp (LSD scaling scheme - ERA40 atm model - Lifton VDM geomagnetic database), we obtained total P_{10fsp} that are $3.42 ± 0.46$ and $3.57 ± 0.21$ at.g^{-1}.yr^{-1} (Table 6) for the worldwide and high-tropical Andes averages, respectively. Those values are 16−17% lower than the current ^{10}Be total production rates in quartz with the same parametrization (WWM $P_{10quartz} = 4.08 ± 0.23$, and HTA $P_{10quartz} = 4.31 ± 0.12$ at.g^{-1}.yr^{-1}). This difference could partially be explained by the respective oxygen content in these two minerals. Indeed, depending on the feldspar species there is between 8 and 14% less oxygen atoms in feldspar than in quartz.

Kober et al. (2005) proposed total ^{10}Be production rate values in feldspars based on cross-calibrations between sanidine and quartz from two samples (CN19S and CN104S) from the Western Cordillera in northern Chile. In the following discussion, we will consider only their results from sample CN19S because, as reported in Kober et al. (2005), the sample CN104 is not pure sanidine (KAlSi$_3$O$_8$) and

Table 5
Major element compositions of feldspar samples. Measurements were done by ICP-OES at the SARM-CRPG facility (Nancy, France). Composition are normalized to remove the relative influence of the lost on ignition. Raw data, trace element composition and measurement uncertainties are available in supplementary data.

Sample	SiO_2 (wt-%)	Al_2O_3 (wt-%)	Fe_2O_3 (wt-%)	MgO (wt-%)	CaO (wt-%)	Na_2O (wt-%)	K_2O (wt-%)	TiO_2 (wt-%)	MnO (wt-%)
CQ1	59.32	25.38	0.26	0.02	8.21	6.27	0.54	0.00	0.00
CQ3	59.62	25.22	0.27	0.02	8.20	6.13	0.53	0.00	0.00
CQ6	59.90	25.03	0.25	0.02	8.16	6.11	0.52	0.00	0.00
CQ8	59.66	25.21	0.26	0.02	8.23	6.09	0.53	0.00	0.00
CQ10	59.78	25.11	0.26	0.02	8.20	6.10	0.53	0.00	0.00
CQ12	58.95	25.63	0.27	0.02	8.38	6.22	0.54	0.00	0.00
CQ18	59.29	25.43	0.26	0.02	8.28	6.19	0.54	0.00	0.00
TM6	59.79	25.10	0.26	0.02	8.17	6.14	0.53	0.00	0.00
Mean Composition[a]	59.5 ± 0.3	25.3 ± 0.2	0.26 ± 0.01	0.02	8.23 ± 0.07	6.16 ± 0.06	0.53 ± 0.01	–	–
TU7C[b]	65.72	20.08	1.01	0.41	5.68	5.17	1.72	0.20	0.00

[a] The mean composition does not include TU7C, the uncertainty corresponds to 1 standard deviation.
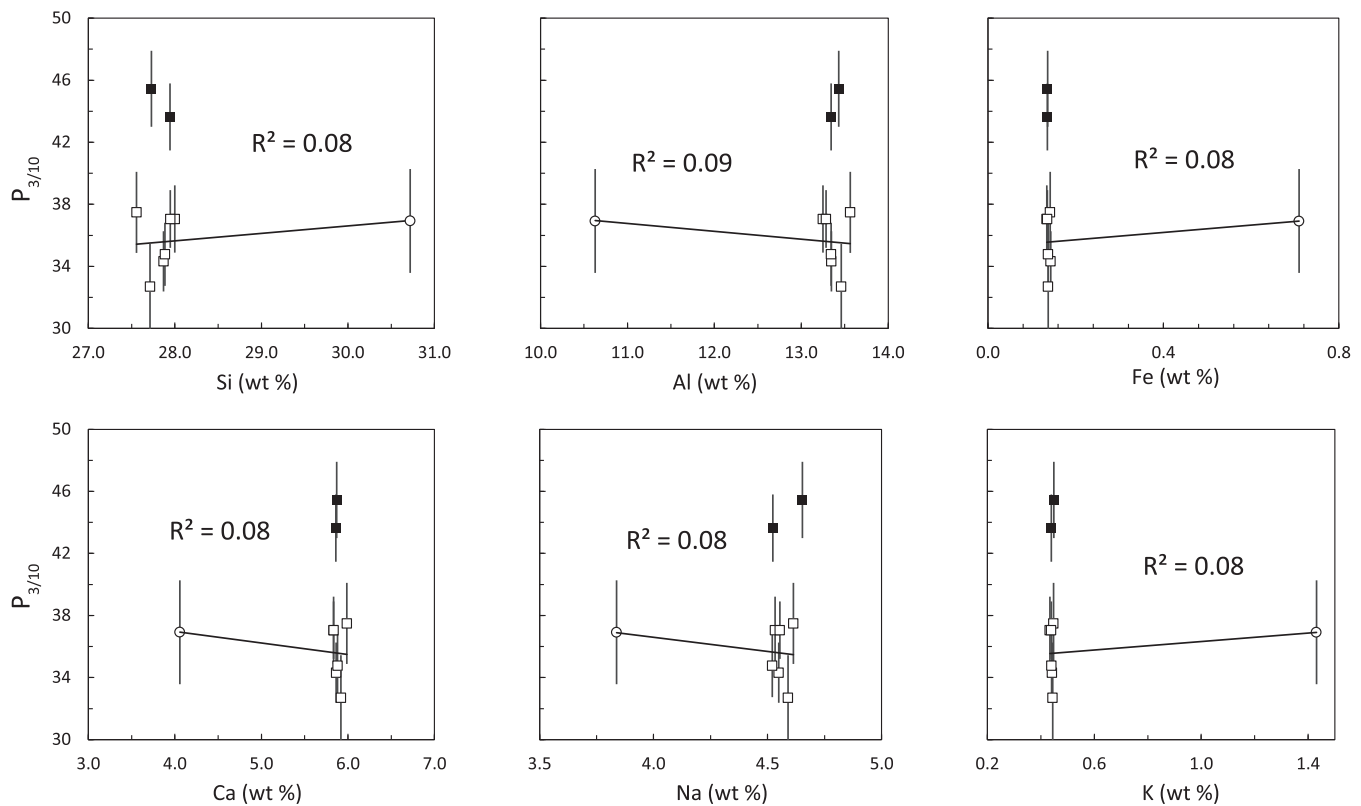[b] Composition normalized from data of Blard et al. (2013a).

Fig. 6. Tentative correlations between $P_{3/10}$ production ratios (calculated for the HTA ^{3}He production rate) and the major element chemical compositions of feldspar (reported in weight fraction). Sample TU7C (Blard et al., 2013a) is plotted as a circle. Sample TU-1A is not included in this analysis because its major element chemical composition was not supplied in Blard et al. (2013a). The two grayed samples are the outliers CQ1 and CQ10, which are therefore not included in the linear regressions.

likely contained about 20% of quartz. They obtained a ^{10}Be sanidine/quartz concentration ratio of 0.77 ± 0.05 for CN19S. Multiplying this value by the recently updated $P_{10quartz}$ as defined above (CREp, Martin et al., 2017), this leads to $P_{10sanidine}$ of 3.16 ± 0.38 and 3.34 ± 0.31 at.g^{-1}.yr^{-1}, for the worldwide and high-tropical Andes averages, respectively. Considering uncertainties, those values are indistinguishable to the P_{10fsp} obtained in our study (Table 5). Interestingly, it suggests again that the chemical composition of feldspars would only have a limited impact on their ^{10}Be *in situ-*production rate variability.

5.4. Geomorphological implications

Absolute timing of landslide sequences is crucial for their understanding in terms of triggering factors, mechanisms of failure, time of recurrence, contribution to regional erosion and relief evolution, etc. (e.g. Crosta and Clague, 2009; Zerathe et al., 2014; Pánek, 2015; Pánek and Klimeš, 2016). Along the western flank of the Andes, numerous giant paleo-landslides have been recognized since a decade (e.g. Audin and Bechir, 2006; Crosta et al., 2014; Mather et al., 2014). However, very few of them have been absolutely dated (Margirier et al., 2015; Crosta et al., 2016), which leaves
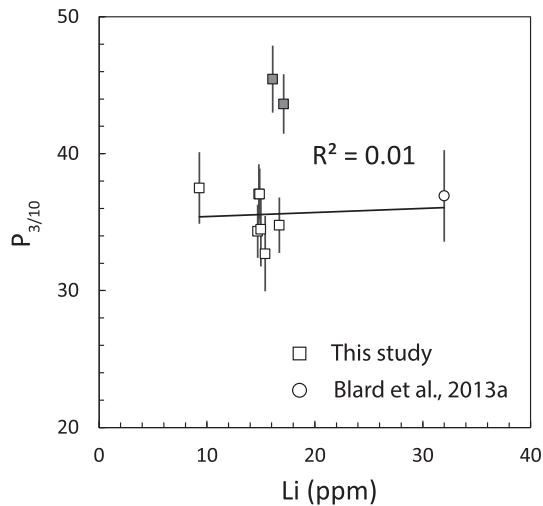
Fig. 7. $P_{3/10}$ production ratios (calculated for the HTA SLHL ^{3}He production rate) versus lithium contents of feldspar. The two grayed samples are the outliers CQ1 and CQ10, which are not included in the linear regression.

open first order debates about how tectonics and climate may control gravitational failures in this hyper-arid region (see for instance the opposed conclusions in McPhillips et al., 2014; Margirier et al., 2015). The main reason for this lack of chronological constraints is that the western Andean landscapes are dominated by volcanic lithologies (e.g. ignimbrite), mostly free of quartz. The proposed new calibration of total ^{10}Be production rate in

feldspars is therefore a promising step towards the improvement of landslide chronologies and understanding of other geomorphological processes in the Western Andes.

Cosmic-ray exposure ages obtained on the Caquilluco landslide complex bring first insights on the failure mechanisms and timing of each individual event in the sequence. The exposure-age distribution, ranging from ca. 110 to 600 ka (Table 3), confirms the morphological interpretation that can be established from the well-preserved landslide morphology. Oldest exposure-ages of 500–600 ka were obtained on the landslide toe which forms an elongated tongue of rock-avalanche deposits (Fig. 1B) that corresponds to the first gravitational failure of the complex. Then, exposure-ages progressively decrease toward the landslide scarp (down to ca. 110 ka) where several lobes of deposits of lesser extent are superimposed (Fig. 1C). Despite not being sufficient to fully reconstruct the landslide chronology, these new chronological constraints confirm that successive and distinct failure episodes occurred on the Caquilluco landslide since 600 ka. They also suggest that those events where separated by at least a few thousands of years. In a near future, this will permit to address the recurrence time of such giant landslides (V > km^3), which is key for understanding the respective role of past climate variations and earthquake recurrence on landslide triggering in that region. Last, the frequency–volume statistics of past landslides may be used to understand and predict the magnitude of new landslides and reactivations.

6. Conclusion

In this paper we investigate the suitability of feldspar minerals

Table 6
Total SLHL ^{10}Be production rates in feldspars based on ^{3}He$_{px}$ - ^{10}Be$_{fsp}$ cross calibrations from the Caquilluco landslide site.

Scaling scheme[a]	Atmosphere Model[b]	Geomagnetic Database[c]	SLHL P_3 in pyroxene[a] (at.g^{-1}.yr^{-1})	SLHL P_{10} in feldspar[d] (at.g^{-1}.yr^{-1})
Lal-Stone time corrected (Lal, 1991; Stone, 2000; Nishiizumi et al., 1989; Balco et al., 2008)	Standard	Atmospheric ^{10}Be-based VDM	WWM 121 ± 15	3.43 ± 0.60
			HTA 125 ± 4	3.53 ± 0.21
		LSD Framework	WWM 116 ± 17	3.29 ± 0.67
			HTA 119 ± 6	3.36 ± 0.24
		Lifton VDM 2016	WWM 118 ± 16	3.34 ± 0.64
			HTA 121 ± 4	3.42 ± 0.20
	ERA40	Atmospheric ^{10}Be-based VDM	WWM 122 ± 13	3.49 ± 0.50
			HTA 137 ± 5	3.84 ± 0.22
		LSD Framework	WWM 118 ± 14	3.35 ± 0.57
			HTA 130 ± 6	3.65 ± 0.27
		Lifton VDM 2016	WWM 120 ± 14	3.40 ± 0.54
			HTA 132 ± 5	3.72 ± 0.22
LSD (Lifton et al., 2014)	Standard	Atmospheric ^{10}Be-based VDM	WWM 121 ± 13	3.46 ± 0.51
			HTA 121 ± 4	3.43 ± 0.20
		LSD Framework	WWM 117 ± 14	3.30 ± 0.56
			HTA 110 ± 4	3.13 ± 0.18
		Lifton VDM 2016	WWM 119 ± 14	3.36 ± 0.54
			HTA 116 ± 4	3.28 ± 0.19
	ERA40	Atmospheric ^{10}Be-based VDM	WWM 123 ± 11	3.52 ± 0.45
			HTA 132 ± 5	3.76 ± 0.22
		LSD Framework	WWM 119 ± 12	3.37 ± 0.48
			HTA 121 ± 5	3.43 ± 0.21
		Lifton VDM 2016	WWM 121 ± 12	3.42 ± 0.46
			HTA 127 ± 5	3.57 ± 0.21

[a] Total cosmogenic ^{3}He production rates are scaled to the reference sea level high latitude (SLHL) position using the calculation procedures and the scaling frameworks reported by Martin et al. (2017). WWM refers to World-Wide Mean production rate and HTA to High elevation Tropical Andes.
[b] The Standard atmosphere model is based on the National Oceanic and Atmospheric Administration (N.O.A.A, 1976) and the ERA-40 reanalysis dataset of Uppala et al. (2005).
[c] Geomagnetic Databases rely on Virtual Dipole Moment (VDM) models and values that are based on (1) Muscheler et al. (2005) and Valet et al. (2005) for the Atmospheric ^{10}Be-based VDM; (2) Lifton et al. (2014) for the LDS framework; and (3) Pavón-Carrasco et al. (2014), Laj et al. (2004) and Ziegler et al. (2011) for the Lifton VDM 2016.
[d] Total SLHL P_{10} in feldspar are obtained by combining the weighted-mean $P_{3/10}$ production ratio with the P_3 in pyroxene scaled for different scheme, atmosphere and geomagnetic reconstruction models (see text for details). Reported errors correspond to external (total) uncertainties at 1σ level and include the propagation of uncertainty associated with the weighted-mean $P_{3/10}$ production ratio and uncertainty associated with SLHL P_3 in pyroxene.

for [10]Be dating. The strategy was to cross-calibrate the total production rate of [10]Be in feldspar against the total production rate of [3]He in pyroxene in the same rock sample. This was performed by measuring the concentration of cosmogenic [3]He and [10]Be in pyroxenes and feldspars respectively, of eight samples of ignimbrite boulders from a giant paleo-landslide located in the high central Andes of Southern Peru (Lat. 18°S). The standard chemical protocol routinely used while processing quartz minerals was revisited to make it efficient for feldspar minerals. In particular, a centrifugation step may be required after HF-dissolution of feldspar in order to remove fluoride precipitates under the form of hydrated colloid gels. As we showed that these colloid gels contain less than 2% of the [9]Be carrier added to feldspar as a spike, they can be removed without significant effect on the Be yield. Then, due to the high quantity of Al release by feldspar dissolution, the cation exchange column chromatography should be repeated if the required purity of Be is not reached after a single separation.

In our analysis of the $^{3}He_{px}$ - $^{10}Be_{fsp}$ production ratios, we included two samples from the Tunupa volcano (high central Andes, lat. 20°S) presented in the dataset of Blard et al. (2013a). Discarding two outliers (CQ1 and CQ10), for which an excess of inherited [3]He was suspected, the $^{3}He_{px}$ - $^{10}Be_{fsp}$ production ratios yield weighted-mean of 35.2 ± 1.4 ($\chi^2_{(95\%)}$=1.32/14.07) and 35.6 ± 0.5 ($\chi^2_{(95\%)}$=3.62/14.07) taking into account the total WWM and the HTA SLHL [3]He production rates, respectively. While theoretically only a minor impact of the compositional variability of feldspar minerals is expected on the [10]Be production rate, definitive conclusions could not be reached from this study because of the low compositional variation of our dataset. This issue remains to be further tested from a larger feldspars chemical composition variability.

Importantly, we detected a non-negligible amount of native [9]Be in our feldspar samples, we thus highly recommend to systematically measure the [9]Be content of the purified grains to avoid any bias in the [10]Be concentration calculations.

Considering the HTA [3]He production rate (CREp), the mean $^{3}He_{px}$ - $^{10}Be_{fsp}$ production ratio obtained in this study allows the determination of a SLHL [10]Be total *in situ*-production rate in feldspar of 3.57 ± 0.21 at.g^{-1}.yr^{-1} (using the LSD scaling scheme, the ERA40 atm model and the VDM of Lifton, 2016).

The possible constraints provided by the measured [10]Be concentrations in feldspar will open, when combined with other TCNs such as [36]Cl that has a significantly smaller half-life, new perspectives to address complex exposure histories (e.g. Wirsig et al., 2016) in geological settings (e.g. mafic environments) where this is currently not possible.

Acknowledgments

Appendix A. Supplementary data

Supplementary data related to this article can be found at http://dx.doi.org/10.1016/j.quageo.2017.06.004.

References

Ackert, R.P., Singer, B.S., Guillou, H., Kaplan, M.R., Kurz, M.D., 2003. Long-term cosmogenic [3]He production rates from [40]Ar/[39]Ar and K-Ar dated Patagonian lava flows at 47°S. Earth Planet. Sci. Lett. 210, 119–136.

Acosta, H., Alván, A., Mamani, M., Oviedo, M., Rodriguez, J., 2010. Geología de los cuadrángulos de Pachía (36-v) y Palca (36-x), escala 1:50 000. INGEMMET, Bol. Ser. A Carta Geol. Nac. 139, 100, 7 mapas.

Al-harbi, B.G., Dahlan, A., Nasser, M., Khaldi, M.H., 2012. Aluminum and iron precipitation during sandstone acidizing using organic-HF acids. In: SPE International Symposium and Exhibition on Formation Damage Control. Society of Petroleum Engineers. January 2012.

Amidon, W.H., Farley, K.A., 2011. Cosmogenic [3]He production rates in apatite, zircon and pyroxene inferred from Bonneville flood erosional surfaces. Quat. Geochronol. 6, 10–21.

Amidon, W.H., Rood, D.H., Farley, K.A., 2009. Cosmogenic [3]He and [21]Ne production rates calibrated against [10]Be in minerals from the Coso volcanic field. Earth Planet. Sci. Lett. 280, 194–204.

Amidon, W.H., Farley, K.A., Burbank, D.W., Pratt-Sitaula, B., 2008. Anomalous cosmogenic [3]He production and elevation scaling in the high Himalaya. Earth Planet. Sci. Lett. 265, 287–301.

Andrews, J.N., 1985. The isotopic composition of radiogenic helium and its use to study groundwater movement in confined aquifers. Chem. Geol. 49, 339–351.

Andrews, J.N., Giles, I.S., Kay, R.L.F., Lee, D.J., Osmond, J.K., Cowart, J.B., Gale, J., 1982. Radioelements, radiogenic helium and age relationships for groundwaters from the granites at Stripa, Sweden. Geochimica Cosmochimica Acta 46, 1533–1543.

Argento, D.C., Reedy, R.C., Stone, J.O., 2013. Modeling the Earth's cosmic radiation. Nucl. Instrum. Methods Phys. Res. Sect. B Beam Interact. Mater. Atoms 294, 464–469.

Arnold, M., Aumaître, G., Bourlès, D.L., Keddaddouche, K., Braucher, R., Finkel, R.C., Nottoli, E., Benedetti, L., Merchel, S., 2013. The French accelerator mass spectrometry facility ASTER after 4 years: status and recent developments on [36]Cl and [129]I. Nucl. Instrum. Methods Phys. Res. Sect. B Beam Interact. Mater. Atoms 294, 24–28.

Arnold, M., Merchel, S., Bourlès, D.L., Braucher, R., Benedetti, L., Finkel, R.C., Aumaître, G., Gottdang, A., Klein, M., 2010. The French accelerator mass spectrometry facility ASTER: improved performance and developments. Nucl. Instrum. Methods Phys. Res. Sect. B Beam Interact. Mater. Atoms 268, 1954–1959.

Athanassas, C.D., Bourlès, D.L., Braucher, R., Druitt, T.H., Nomikou, P., Léanni, L., 2016. Evidence from cosmic-ray exposure (CRE) dating for the existence of a pre-Minoan caldera on Santorini, Greece. Bull. Volcanol. 78, 1–13.

Audin, L., Bechir, A., 2006. Active tectonics as determinant factor in landslides along the Western Cordillera. Congr. Peruano de Geol. 13, 17–20.

Balco, G., Briner, J., Finkel, R.C., Rayburn, J.A., Ridge, J.C., Schaefer, J.M., 2009. Regional beryllium-10 production rate calibration for late-glacial northeastern North America. Quat. Geochronol. 4, 93–107.

Balco, G., Stone, J.O., Lifton, N.A., Dunai, T.J., 2008. A complete and easily accessible means of calculating surface exposure ages or erosion rates from [10]Be and [26]Al measurements. Quat. Geochronol. 3, 174–195.

Blard, P.-H., Balco, G., Burnard, P.G., Farley, K.A., Fenton, C.R., Friedrich, R., Jull, A.J.T., Niedermann, S., Pika, R., Schaefer, J.M., Scott, E.M., Shuster, D.L., Stuart, F.M., Stute, M., Tibari, B., Winckler, G., Zimmermann, L., 2015. An inter-laboratory comparison of cosmogenic [3]He and radiogenic [4]He in the CRONUS-P pyroxene standard. Quat. Geochronol. 26, 11–19.

Blard, P.-H., Braucher, R., Lavé, J., Bourlès, D., 2013a. Cosmogenic [10]Be production rate calibrated against [3]He in the high Tropical Andes (3800–4900 m, 20–22 S). Earth Planet. Sci. Lett. 382, 140–149.

Blard, P.-H., Lavé, J., Sylvestre, F., Placzek, C.J., Claude, C., Galy, V., Tibari, B., 2013b. Cosmogenic [3]He production rate in the high tropical Andes (3800 m, 20 S): implications for the local last glacial maximum. Earth Planet. Sci. Lett. 377, 260–275.

Blard, P.-H., Farley, K.A., 2008. The influence of radiogenic [4]He on cosmogenic [3]He determinations in volcanic olivine and pyroxene. Earth Planet. Sci. Lett. 276, 20–29.

Blard, P.-H., Lavé, J., Pik, R., Quidelleur, X., Bourlès, D.L., Kieffer, G., 2005. Fossil cosmogenic [3]He record from K-Ar dated basaltic flows of Mount Etna volcano (Sicily, 38°N): evaluation of a new paleoaltimeter. Earth Planet. Sci. Lett. 236, 613–631.

Blard, P.-H., Pik, R., Lavé, J., Bourlès, D.L., Burnard, P.G., Yokochi, R., Marty, B., Trusdell, F., 2006. Cosmogenic [3]He production rates revisited from evidences of grain size dependent release of matrix-sited helium. Earth Planet. Sci. Lett. 247, 222–234.

Borchers, B., Marrero, S., Balco, G., Caffee, M., Goehring, B., Lifton, N., Stone, J., 2016. Geological calibration of spallation production rates in the CRONUS-Earth project. Quat. Geochronol. 31, 188–198.

Braucher, R., Bourlès, D., Merchel, S., Romani, J.V., Fernandez-Mosquera, D., Marti, K.,

Keddadouche, K., 2013. Determination of muon attenuation lengths in depth profiles from in situ produced cosmogenic nuclides. Nucl. Instrum. Methods Phys. Res. Sect. B Beam Interact. Mater. Atoms 294, 484−490.

Braucher, R., Merchel, S., Borgomano, J., Bourlès, D.L., 2011. Production of cosmogenic radionuclides at great depth: a multi element approach. Earth Planet. Sci. Lett. 309, 1−9.

Bromley, G.R., Winckler, G., Schaefer, J.M., Kaplan, M.R., Licht, K.J., Hall, B.L., 2014. Pyroxene separation by HF leaching and its impact on helium surface-exposure dating. Quat. Geochronol. 23, 1−8.

Brown, E.T., Stallard, R.F., Larsen, M.C., Raisbeck, G.M., Yiou, F., 1995. Denudation rates determined from the accumulation of in situ-produced ^{10}Be in the Luquillo experimental forest, Puerto Rico. Earth Planet. Sci. Lett. 129, 193−202.

Brown, E.T., Edmond, J.M., Raisbeck, G.M., Yiou, F., Kurz, M.D., Brook, E.J., 1991. Examination of surface exposure ages of moraines in Arena Valley, Antarctica using in situ produced ^{10}Be and ^{26}Al. Geochimica Cosmochimica Acta 55, 2269−2283.

Cerling, T.E., Craig, H., 1994. Cosmogenic ^{3}He production rates from 39°N to 46°N latitude, western USA and France. Geochimica Cosmochimica Acta 58, 249−255.

Chmeleff, J., von Blanckenburg, F., Kossert, K., Jakob, D., 2010. Determination of the ^{10}Be half-life by multicollector ICP-MS and liquid scintillation counting. Nucl. Instrum. Methods Phys. Res. Sect. B Beam Interact. Mater. Atoms 268, 192−199.

Clifton, T., Granger, D.E., Gilbert, Z., Caffee, M., 2005. Quartz sample preparation for AMS. In: The 10th International Conference on Accelerator Mass Spectrometry. September 2005.

Corbett, L.B., Bierman, P.R., Rood, D.H., 2016. An approach for optimizing *in-situ* cosmogenic ^{10}Be sample preparation. Quat. Geochronol. 33, 24−34.

Crosta, G.B., Hermanns, R.L., Dehls, J., Lari, S., Sepulveda, S., 2016. Rock avalanches clusters along the northern Chile coastal scarp. Geomorphology. http://dx.doi.org/10.1016/j.geomorph.2016.11.024 (in press).

Crosta, G.B., Paolo, F., Elena, V., Hermanns, R.L., 2015. The cerro caquilluco−cerrillos Negros giant rock avalanches (Tacna, Peru). Eng. Geol. Soc. Territ. 2, 921−924.

Crosta, G.B., Hermanns, R.L., Frattini, P., Valbuzzi, E., Valagussa, A., 2014. Large slope instabilities in Northern Chile: inventory, characterisation and possible triggers. In: Proceedings of the 3rd World Landslide Forum, 2−6 June 2014, Bejing, p. 6. http://dx.doi.org/10.1007/978/-3-319-04996-0_28.

Crosta, G.B., Clague, J.J., 2009. Dating, triggering, modelling, and hazard assessment of large landslides. Geomorphology 2009, 1−4. http://dx.doi.org/10.1016/j.geomorph.2008.04.007.

Delunel, R., Blard, P.-H., Martin, L.C., Nomade, S., Schlunegger, F., 2016. Long term low latitude and high elevation cosmogenic ^{3}He production rate inferred from a 107 ka-old lava flow in northern Chile; 22° S-3400m a.s.l. Geochimica Cosmochimica Acta 184, 71−87.

Dunai, T.J., 2010. Cosmogenic Nuclides: Principles, Concepts and Applications in the Earth Surface Sciences. Cambridge University Press.

Dunai, T.J., Stuart, F.M., Pik, R., Burnard, P., Gayer, E., 2007. Production of ^{3}He in crustal rocks by cosmogenic thermal neutrons. Earth Planet. Sci. Lett. 258, 228−236.

Dunai, T.J., Wijbrans, J.R., 2000. Long-term cosmogenic ^{3}He production rates (152 ka-1.35 Ma) from ^{40}Ar/^{39}Ar dated basalt flows at 29°N latitude. Earth Planet. Sci. Lett. 176, 147−156.

Dunne, J., Elmore, D., Muzikar, P., 1999. Scaling factors for the rates of production of cosmogenic nuclides for geometric shielding and attenuation at depth on sloped surfaces. Geomorphology 27, 3−11.

Evenstar, L.A., Hartley, A.J., Stuart, F.M., Mather, A.E., Rice, C.M., Chong, G., 2009. Multiphase development of the Atacama Planation Surface recorded by cosmogenic ^{3}He exposure ages: implications for uplift and Cenozoic climate change in western South America. Geology 37, 27−30.

Farley, K.A., Libarkin, J., Mukhopadhyay, S., Amidon, W., 2006. Cosmogenic and nucleogenic ^{3}He in apatite, titanite, and zircon. Earth Planet. Sci. Lett. 248, 451−461.

Fenton, C.R., Niedermann, S., 2014. Surface exposure dating of young basalts (1-200 ka) in the San Francisco volcanic field (Arizona, USA) using cosmogenic ^{3}He and ^{21}Ne. Quat. Geochronol. 19, 87−105.

Fenton, C.R., Hermanns, R.L., Blikra, L.H., Kubik, P.W., Bryant, C., Niedermann, S., Goethals, M.M., 2011. Regional ^{10}Be production rate calibration for the past 12ka deduced from the radiocarbon-dated Grøtlandsura and Russenes rock avalanches at 69°N, Norway. Quat. Geochronol. 6, 437−452.

Foeken, J.P.T., Stuart, F.M., Mark, D.F., 2012. Long-term low latitude cosmogenic ^{3}He production rate determined from a 126 ka basalt from Fogo, Cape Verdes. Earth Planet. Sci. Lett. 359, 14−25.

Gayer, E., Pik, R., Lavé, J., France-Lanord, C., Bourlès, D., Marty, B., 2004. Cosmogenic ^{3}He in Himalayan garnets indicating an altitude dependence of the ^{3}He/^{10}Be production ratio. Earth Planet. Sci. Lett. 229, 91−104.

Goehring, B.M., Kurz, M.D., Balco, G., Schaefer, J.M., Licciardi, J., Lifton, N., 2010. A reevaluation of in situ cosmogenic ^{3}He production rates. Quat. Geochronol. 5, 410−418.

Gosse, J.C., Phillips, F.M., 2001. Terrestrial in situ cosmogenic nuclides: theory and application. Quat. Sci. Rev. 20, 1475−1560.

Hall, S.R., Farber, D.L., Audin, L., Finkel, R.C., 2012. Recently active contractile deformation in the forearc of southern Peru. Earth Planet. Sci. Lett. 337, 85−92.

Iacumin, P., Quercioli, J., 1993. A new technique for quantitative separation of quartz from feldspars. Eur. J. Mineralogy 5, 677−678.

Kelly, M.A., Lowell, T.V., Applegate, P.J., Phillips, F.M., Schaefer, J.M., Smith, C.A., Hudson, A.M., 2015. A locally calibrated, late glacial ^{10}Be production rate from a low-latitude, high-altitude site in the Peruvian Andes. Quat. Geochronol. 26, 70−85.

Kober, F., Ivy-Ochs, S., Leya, I., Baur, H., Magna, T., Wieler, R., Kubik, P.W., 2005. In situ cosmogenic ^{10}Be and ^{21}Ne in sanidine and in situ cosmogenic ^{3}He in Fe−Ti-oxide minerals. Earth Planet. Sci. Lett. 236, 404−418.

Korschinek, G., Bergmaier, A., Faestermann, T., Gerstmann, U.C., Knie, K., Rugel, G., Kossert, K., 2010. A new value for the half-life of ^{10}Be by heavy-ion elastic recoil detection and liquid scintillation counting. Nucl. Instrum. Methods Phys. Res. Sect. B Beam Interact. Mater. Atoms 268, 187−191.

Kurz, M.D., 1986. In situ production of terrestrial cosmogenic helium and some applications to geochronology. Geochimica Cosmochimica Acta 50, 2855−2862.

Laj, C., Kissel, C., Beer, J., 2004. High Resolution Global Paleointensity Stack since 75 Kyr (GLOPIS-75) Calibrated to Absolute Values, in Timescales of the Paleomagnetic Field, 2004, pp. 255−265. http://dx.doi.org/10.1029/145GM19.

Lal, D., 1991. Cosmic ray labeling of erosion surfaces: in situ nuclide production rates and erosion models. Earth Planet. Sci. Lett. 104, 424−439.

Licciardi, J.M., Kurz, M.D., Curtice, J.M., 2006. Cosmogenic ^{3}He production rates from Holocene lava flows in Iceland. Earth Planet. Sci. Lett. 246, 251−264.

Licciardi, J.M., Kurz, M.D., Clark, P.U., Brook, E.J., 1999. Calibration of cosmogenic ^{3}He production rates from Holocene lava flows in Oregon, USA, and effects of the Earth's magnetic field. Earth Planet. Sci. Lett. 172, 261−271.

Lifton, N., 2016. Implications of two Holocene time-dependent geomagnetic models for cosmogenic nuclide production rate scaling. Earth Planet. Sci. Lett. 433, 257−268.

Lifton, N., Sato, T., Dunai, T.J., 2014. Scaling in situ cosmogenic nuclide production rates using analytical approximations to atmospheric cosmic-ray fluxes. Earth Planet. Sci. Lett. 386, 149−160.

Margirier, A., Audin, L., Carcaillet, J., Schwartz, S., 2015. Tectonic and climatic controls on the Chuquibamba landslide (western Andes, southern Peru). Earth Surf. Dyn. Discuss. 2, 1129−1153.

Marrero, S.M., Phillips, F.M., Caffee, M.W., Gosse, J.C., 2016. CRONUS-Earth cosmogenic ^{36}Cl calibration. Quat. Geochronol. 31, 199−219.

Martin, L.C.P., Blard, P.-H., Balco, G., Lavé, J., Delunel, R., Lifton, N., Laurent, V., 2017. The CREp program and the ICE-D production rate calibration database: a fully parameterizable and updated online tool to compute cosmic-ray exposure ages. Quat. Geochronol. 38, 25−49 quageo.2016.11.006.

Martin, L.C.P., Blard, P.-H., Lavé, J., Braucher, R., Lupker, M., Condom, Charreau, J., Mariotti, V., , ASTER Team, Davy, E., 2015. In situ cosmogenic ^{10}Be production rate in the high tropical Andes. Quat. Geochronol. 30, 54−68.

Masarik, J., Kim, K.J., Reedy, R.C., 2007. Numerical simulations of in situ production of terrestrial cosmogenic nuclides. Nucl. Instrum. Methods Phys. Res. Sect. B Beam Interact. Mater. Atoms 259, 642−645.

Masarik, J., 2002. Numerical simulation of in situ production of cosmogenic nuclides. Geochimica Cosmochimica Acta 66, A491.

Mather, A.E., Hartley, A.J., Griffiths, J.S., 2014. The giant coastal landslides of Northern Chile: tectonic and climate interactions on a classic convergent plate margin. Earth Planet. Sci. Lett. 388, 249−256.

Matsuda, J., Matsumoto, T., Sumino, H., Nagao, K., Yamamoto, J., Miura, Y., Sano, Y., 2002. The ^{3}He/^{4}He ratio of the new internal He Standard of Japan (HESJ). Geochem. J. 36, 191−195.

McIntyre, G.A., Brooks, C., Compston, W., Turek, A., 1966. The statistical assessment of Rb-Sr isochrons. J. Geophys. Res. 71, 5459−5468.

McPhillips, D., Bierman, P.R., Rood, D.H., 2014. Millennial-scale record of landslides in the Andes consistent with earthquake trigger. Nat. Geosci. 7, 925−930.

Merchel, S., Arnold, M., Aumaitre, G., Benedetti, L., Bourlès, D.L., Braucher, R., Alfimov, V., Freeman, S.P.H.T., Steier, P., Wallner, A., 2008. Towards more precise ^{10}Be and ^{36}Cl data from measurements at the 10^{-14} level: influence of sample preparation. Nucl. Instrum. Methods Phys. Res. Sect. B Beam Interact. Mater. Atoms 266, 4921−4926.

Muscheler, R., Beer, J., Kubik, P.W., Synal, H.A., 2005. Geomagnetic field intensity during the last 60,000 years based on ^{10}Be and ^{36}Cl from the Summit ice cores and ^{14}C. Quat. Sci. Rev. 24, 1849−1860.

N.O.A.A, 1976. U.S. Standard Atmosphere. US Gov. Print. Off.

Nishiizumi, K., Imamura, M., Caffee, M.W., Southon, J.R., Finkel, R.C., McAninch, J., 2007. Absolute calibration of ^{10}Be AMS standards. Nucl. Instrum. Methods Phys. Res. Sect. B Beam Interact. Mater. Atoms 258, 403−413.

Nishiizumi, K., Caffee, M.W., Finkel, R.C., Brimhall, G., Mote, T., 2005. Remnants of a fossil alluvial fan landscape of Miocene age in the Atacama Desert of northern Chile using cosmogenic nuclide exposure age dating. Earth Planet. Sci. Lett. 237, 499−507.

Nishiizumi, K., Winterer, E.L., Kohl, C.P., Klein, J., Middleton, R., Lal, D., Arnold, J.R., 1989. Cosmic ray production rates of ^{10}Be and ^{26}Al in quartz from glacially polished rocks. J. Geophys. Res. Solid Earth 94, 17907−17915.

Pánek, T., Klimeš, J., 2016. Temporal behavior of deep-seated gravitational slope deformations: a review. Earth-Science Rev. 156, 14−38.

Pánek, T., 2015. Recent progress in landslide dating: a global overview. Prog. Phys. Geogr. 3, 168−198.

Pavón-Carrasco, F.J., Osete, M.L., Torta, J.M., De Santis, A., 2014. A geomagnetic field model for the Holocene based on archaeomagnetic and lava flow data. Earth Planet. Sci. Lett. 388, 98−109.

Phillips, F.M., Argento, D.C., Balco, G., Caffee, M.W., Clem, J., Dunai, T.J., Finkel, R., Goehring, B., Gosse, J.C., Hudsonj, A.M., Jull, A.J.T., Kelly, M.A., Kurz, M., Lal, D., Lifton, N., Marrero, S.M., Nishiizumi, K., Reedy, R.C., Schaefer, J., Stone, J.O.H., Swanson, T., Zreda, M.G., 2016. The CRONUS-Earth project: a synthesis. Quat. Geochronol. 31, 119−154.

Phillips, F.M., Stone, W.D., Fabryka-Martin, J.T., 2001. An improved approach to calculating low-energy cosmic-ray neutron fluxes near the land/atmosphere interface. Chem. Geol. 175, 689–701.

Placzek, C.J., Matmon, A., Granger, D.E., Quade, J., Niedermann, S., 2010. Evidence for active landscape evolution in the hyperarid Atacama from multiple terrestrial cosmogenic nuclids. Earth Planet. Sci. Lett. 295, 12–20.

Poreda, R.J., Cerling, T.E., 1992. Cosmogenic neon in recent lavas from the western United States. Geophys. Res. Lett. 19, 1863–1866.

Portenga, E.W., Bierman, P.R., Duncan, C., Corbett, L.B., Kehrwald, N.M., Rood, D.H., 2015. Erosion rates of the Bhutanese Himalaya determined using in situ-produced ^{10}Be. Geomorphology 233, 112–126.

Quang, C.X., Clark, A.H., Lee, J.K., Hawkes, N., 2005. Response of supergene processes to episodic Cenozoic uplift, pediment erosion, and ignimbrite eruption in the porphyry copper province of southern Peru. Econ. Geol. 100, 87–114.

Scarsi, P., 2000. Fractional extraction of helium by crushing of olivine and clino-pyroxene phenocrysts: effects on the ^{3}He/^{4}He measured ratio. Geochimica Cosmochimica Acta 64, 3751–3762.

Schimmelpfennig, I., Williams, A., Pik, R., Burnard, P., Niedermann, S., Finkel, R., Schneider, B., Benedetti, L., 2011. Inter-comparison of cosmogenic in-situ ^{3}He, ^{21}Ne and ^{36}Cl at low latitude along an altitude transect on the SE slope of Kilimanjaro volcano (3°S, Tanzania). Quat. Geochronol. 6, 425–436.

Schimmelpfennig, I., Benedetti, L., Finkel, R., Pik, R., Blard, P.-H., Bourlès, D., Burnard, P., Williams, A., 2009. Sources of in-situ ^{36}Cl in basaltic rocks. Implications for calibration of production rates. Quat. Geochronol. 4, 441–461.

Stone, J.O., 2000. Air pressure and cosmogenic isotope production. J. Geophys. Res. Solid Earth 105, 23753–23759.

Tosdal, R.M., Farrar, E., Clark, A.H., 1981. K-Ar geochronology of the late Cenozoic volcanic rocks of the Cordillera Occidental, southernmost Peru. J. Volcanol. Geotherm. Res. 10, 157–173.

Uppala, S.M., KÅllberg, P.W., Simmons, A.J., Andrae, U., Bechtold, V.D.C., Fiorino, M., Gibson, J.K., Haseler, J., Hernandez, A., Kelly, G.A., Li, X., Onogi, K., Saarinen, S., Sokka, N., Allan, R.P., Andersson, E., Arpe, K., Balmaseda, M.A., Beljaars, A.C.M., Van De Berg, L., Bidlot, J., Bormann, N., Caires, S., Chevallier, F., Dethof, A., Dragosavac, M., Fisher, M., Fuentes, M., Hagemann, S., Hólm, E., Hoskins, B.J., Isaksen, L., Janssen, P.A.E.M., Jenne, R., Mcnally, A.P., Mahfouf, J.-F., Morcrette, J.-J., Rayner, N.A., Saunders, R.W., Simon, P., Sterl, A., Trenberth, K.E., Untch, A., Vasiljevic, D., Viterbo, P., Woollen, J., 2005. The ERA-40 re-analysis. Q. J. R. Meteorological Soc. 131, 2961–3012. http://dx.doi.org/10.1256/qj.04.176.

Valet, J.P., Meynadier, L., Guyodo, Y., 2005. Geomagnetic dipole strength and reversal rate over the past two million years. Nature 435, 802–805.

von Blanckenburg, F., 2005. The control mechanisms of erosion and weathering at basin scale from cosmogenic nuclides in river sediment. Earth Planet. Sci. Lett. 237, 462–479.

Ward, G.K., Wilson, S.R., 1978. Procedures for comparing and combining radio-carbon age determinations: a critique. Archaeometry 1, 19–31.

Wirsig, C., Ivy-Ochs, S., Akçar, N., Lupker, M., Hippe, K., Wacker, L., Vockenhuber, C., Schlüchter, C., 2016. Combined cosmogenic ^{10}Be, in situ ^{14}C and ^{36}Cl concentrations constrain Holocene history and erosion depth of Grueben glacier (CH). Swiss J. Geosciences 109, 379–388.

Wörner, G., Uhlig, D., Kohler, I., Seyfried, H., 2002. Evolution of the West Andean Escarpment at 18°S (N. Chile) during the last 25 Ma: uplift, erosion and collapse through time. Tectonophysics 34, 183–198.

Zerathe, S., Lebourg, T., Braucher, R., Bourlès, D., 2014. Mid-Holocene cluster of large-scale landslides revealed in the Southwestern Alps by ^{36}Cl dating. Insight on an Alpine-scale landslide activity. Quat. Sci. Rev. 90, 106–127.

Ziegler, L.B., Constable, C.G., Johnson, C.L., Tauxe, L., 2011. PADM2M: a penalized maximum likelihood model of the 0–2 Ma palaeomagnetic axial dipole moment. Geophys. J. Int. 184, 1069–1089.

Zimmermann, L., Blard, P.-H., Burnard, P., Medynski, S., Pik, R., Puchol, N., 2012. A new single vacuum furnace design for cosmogenic ^{3}He dating. Geostand. Geoanalytical Res. 36, 121–129.